This is a preprint of an article submitted to *Journal of Geophysical Research: Planets* and uploaded to EarthArXiv in November 2024. Subsequent versions of this preprint may differ in content. If accepted, this preprint will be linked to the final published article.

Micro-CT Characterization of the Chang'e 5 Lunar Regolith Samples

Huanyu Wu[1,2], Yuan Zou[1,2], Chi Zhang[3], Wei Yang[3], Bo Wu[2,4], Kai-Leung Yung[2,5], and Qi Zhao[1,2*]

[1]Department of Civil and Environmental Engineering, The Hong Kong Polytechnic University, Hong Kong SAR, China

[2]Research Centre for Deep Space Explorations, The Hong Kong Polytechnic University, Hong Kong SAR, China

[3]Key Laboratory of Earth and Planetary Physics, Institute of Geology and Geophysics, Chinese Academy of Sciences, Beijing, China

[4]Department of Land Surveying and Geo-Informatics, The Hong Kong Polytechnic University, Hong Kong SAR, China

[5]Department of Industrial and Systems Engineering, The Hong Kong Polytechnic University, Hong Kong SAR, China

Corresponding author: Qi Zhao (qi.qz.zhao@polyu.edu.hk)

Key Points:

- The largest dataset of Chang'e 5 lunar regolith particles created by X-ray micro-computed tomography and machine learning-based analysis.
- Three-dimensional density distribution obtained through X-ray micro-computed tomography enables particle-scale mineral identification.
- Chang'e-5 lunar regolith has a lower mean aspect ratio than the Apollo 11, 16 and Luna 16, 20 and 24 samples.

Keywords

Lunar regolith, X-ray micro-CT, Particle size distribution, Particle shape, Spherical harmonic analysis, Lunar regolith maturity

Abstract

Chang'e-5 (CE-5) lunar regolith samples were scanned using X-ray micro-computed tomography (micro-CT), and over 0.7 million particles were extracted from the images through machine learning-based segmentation. This is the largest three-dimensional (3D) image dataset on lunar regolith particles to date, offering a unique opportunity to study the key characteristics of lunar regolith. The image intensity was correlated with mineral density, allowing for the assessment of the bulk density (1.58 g/cm^3), true density (3.17 g/cm^3), and mineralogy of the lunar regolith. Glass and plagioclase contributed 45.6 wt.% of the samples, while pyroxene and olivine made up 49.7 wt.%, and ilmenite accounted for 4.7 wt.%. The median grain size of CE-5 was 57.5 μm, smaller than the Apollo 11, 16 and Luna 16, 20 and 24 samples. Spherical harmonic (SH) analysis and axial ratio (AR) measurement revealed that the CE-5 lunar regolith particles have more complex shapes than two common terrestrial soils and exhibit less spherical shapes than Apollo 11, 16 and Luna 16, 20 and 24 samples. We recommend using size and shape characteristics cautiously when inferring lunar regolith maturity because the intrinsic crystal size of the protolith and complex lunar surface weathering can cause significant size and shape variations. Additionally, characterizing particle shapes requires a large sample size (>1000) to avoid skewed results from outliers. Our non-destructive examination method offers a novel and appealing approach for analyzing critical physical, mineralogical, and morphological properties of million-scale extraterrestrial soil particles, paving the way for future deep space explorations.

Plain Language Summary

Characterizing lunar regolith is crucial for understanding the geological history of the Moon and future resource utilization and base construction on the Moon. By combining X-ray micro-computed tomography and advanced machine learning-based image processing techniques, we were able to extract more than 700,000 lunar regolith particles from the Chang'e-5 lunar regolith samples, which is the largest three-dimensional image dataset on lunar regolith particles so far. This unique dataset allows the non-destructive and more reliable evaluation of the particle size distribution, mineralogy and particle shape characteristics of the Chang'e 5 lunar regolith samples. We found that the Chang'e 5 lunar regolith particles exhibit more complex shapes than typical terrestrial soils and are less spherical compared to the Apollo 11, 16 and Luna 16, 20 and 24 samples. This study not only expanded our knowledge of lunar regolith by obtaining a more comprehensive dataset but also introduced a non-destructive workflow for studying extraterrestrial geomaterials, which will be beneficial for future deep space explorations.

1 Introduction

Lunar exploration has become a global focal point in the field of deep space exploration. Numerous countries and private entities are investing heavily in related technologies and missions. Notable examples include NASA's Artemis program (Smith et al., 2020) and China National Space Administration's Chang'e (CE) Project (Li et al., 2019). These exploration programs are driven by the desire to promote in-situ resource utilization and assess the feasibility of human habitation on the Moon.

On December 1, 2020, China's Chang'e-5 (CE-5) probe landed on a flat area at 43.06°N, 51.92°W in Northern Oceanus Procellarum (Wu et al., 2018). On December 17, 2020, 1731 g of lunar regolith, which included 1500 g collected by the lunar surface sampling and packing system developed by the co-author Professor K. L. Yung's team, was brought back to Earth. The landing site is one of the youngest mare basalts on the Moon with an estimated age of approximately two billion years (Morota et al., 2011; Tian et al., 2021), which is rather away from the previous nine sampling sites accomplished by NASA's Apollo missions and the USSR's Lunar missions, making the CE-5 lunar samples unique in many aspects including their chemical composition and weathering history (Qian et al., 2020; Tian et al., 2021; C. Li et al., 2022; Lu et al., 2023).

Lunar regolith refers to the fine-grained layer on the Moon that is primarily formed by constant micrometeorite impacts (Zhang et al., 2023). Examination of lunar regolith samples could provide valuable insights into various aspects of the Moon's geological history, including the composition and structure of the lunar mantle (Longhi, 1992; Wieczorek, 2006), mare volcanism (Borg et al., 2011; Snape et al., 2019; Tian et al., 2021), and surface processes such as space weathering (Gu et al., 2022; Thompson et al., 2016). Additionally, lunar regolith plays a vital role in lunar base construction and in-situ resource utilization, which not only acts as a natural foundation soil on the Moon (Carrier III et al., 1972; Costes et al., 1971; Perkins & Madson, 1996), but also has the potential to be used as a construction material for habitats, roads, landing pads, and other infrastructure (Ellery, 2022). Therefore, understanding its physical properties is essential for in-situ resource utilization. Recent studies on lunar regolith, specifically the analysis of CE-5 lunar samples, have significantly advanced our understanding of its properties (Chang et al., 2023; Chen et al., 2023; Li et al., 2022; Wu et al., 2024; Xian et al., 2023; Yang et al., 2022; Yao et al., 2022; Zhang et al., 2022). The CE-5 samples have been proven to primarily consist of basalt and mineral fragments, impact melt breccia, agglutinates, and glasses (Chen et al., 2023; Zong et al., 2022). Extensive measurements have been conducted on CE-5 samples to evaluate its physical properties including size distribution, density and specific surface area (Li et al., 2022; Zhang et al., 2022). The particle shape characteristics of lunar regolith are another important physical attribute that not only directly determines its mechanical behavior (Cho et al., 2006; Rousé et al.,

2008) but also records the long-term space weathering (Tsuchiyama et al., 2022; Weber et al., 2020) and solar wind irradiation (Laczniak et al., 2021).

X-ray micro-computed tomography (micro-CT), as a widely-used non-destructive testing approach (Chen et al., 2021; Zhao et al., 2020; Lei et al., 2018), has been employed to conduct grain-scale observations of lunar regolith samples. Matsushima et al. (2008) and Katagiri et al. (2015) studied tens of Apollo 16 lunar regolith particles by micro-CT and established a particle flow model based on the real particle shapes. Chiaramonti et al. (2017) examined the full 3D shapes of Apollo regolith particles using micro-CT and described the particles with spherical harmonic (SH) analysis. Nie et al. (2023) employed micro-CT to quantify the shape characteristics of 224 CE-5 lunar regolith particles and predicted the residual friction angle of lunar regolith. However, it is important to acknowledge that a limited number of particles may not sufficiently represent the diverse characteristics of lunar regolith and potentially lead to skewed or incomplete findings. Although dynamic image analysis (Deitrick & Cannon, 2022; Wilkerson et al., 2024) and laser diffraction (Zhang et al., 2022) have demonstrated the ability to analyze the two-dimensional shape parameters of thousands of lunar regolith particles, these methods still cannot precisely reconstruct the three-dimensional (3D) surface geometry and internal structures of lunar soil particles.

In this study, we utilized X-ray micro-CT to examine the CE-5 lunar regolith samples. The grayscale micro-CT images were processed using machine learning-based segmentation methods, enabling the characterization of more than 0.7 million lunar regolith particles. Furthermore, the physical, morphological, and mineralogical properties of the regolith particles were quantitatively assessed, including particle size distribution, density, mineral content and particle shape characteristics.

2 Materials and Methods

2.1 Chang'e 5 Lunar Regolith Samples and Micro-CT

The lunar regolith samples we examined in this study are CE5C0100YJFM00103 (Figure 1a). Approximately 80 mg of the samples was enclosed in a long tube with an inner diameter of 2 mm (Figure 1b). A FEI HeliScan micro-CT was used to scan a 2 mm high region of interest within the tube with a spatial resolution of 0.99 μm. The voltage for the micro-CT scan is 80 kV and the current is 100 μA. Exposure time is 3.3 s for each frame and 8 frames were averaged for each two-dimensional (2D) radiograph, and the whole scan took approximately 30 hours for 3060 radiographs from different angles. A 2-mm aluminum X-ray beam filter was used to reduce beam hardening artifacts. This non-destructive testing method maximized the utilization of the lunar regolith sample while minimizing any disturbance to its integrity. The 2D micro-CT radiographs were then reconstructed into a 3D digital volume representing the 6.28 mm^3 lunar regolith by FEI Heliscan Micro-CT proprietary reconstruction software (Figure 1c and 1d), with the following settings: automatic beam hardening correction, an automatic ring artifact reduction, and a manual scan optimization that compensates for small drifts of the specimen during the scan and accurately locates the center of reconstruction. The 16-bit raw reconstructed grayscale images were converted into 8-bit, which preserves sufficient information for our further analysis and reduces the memory requirement for image segmentation.

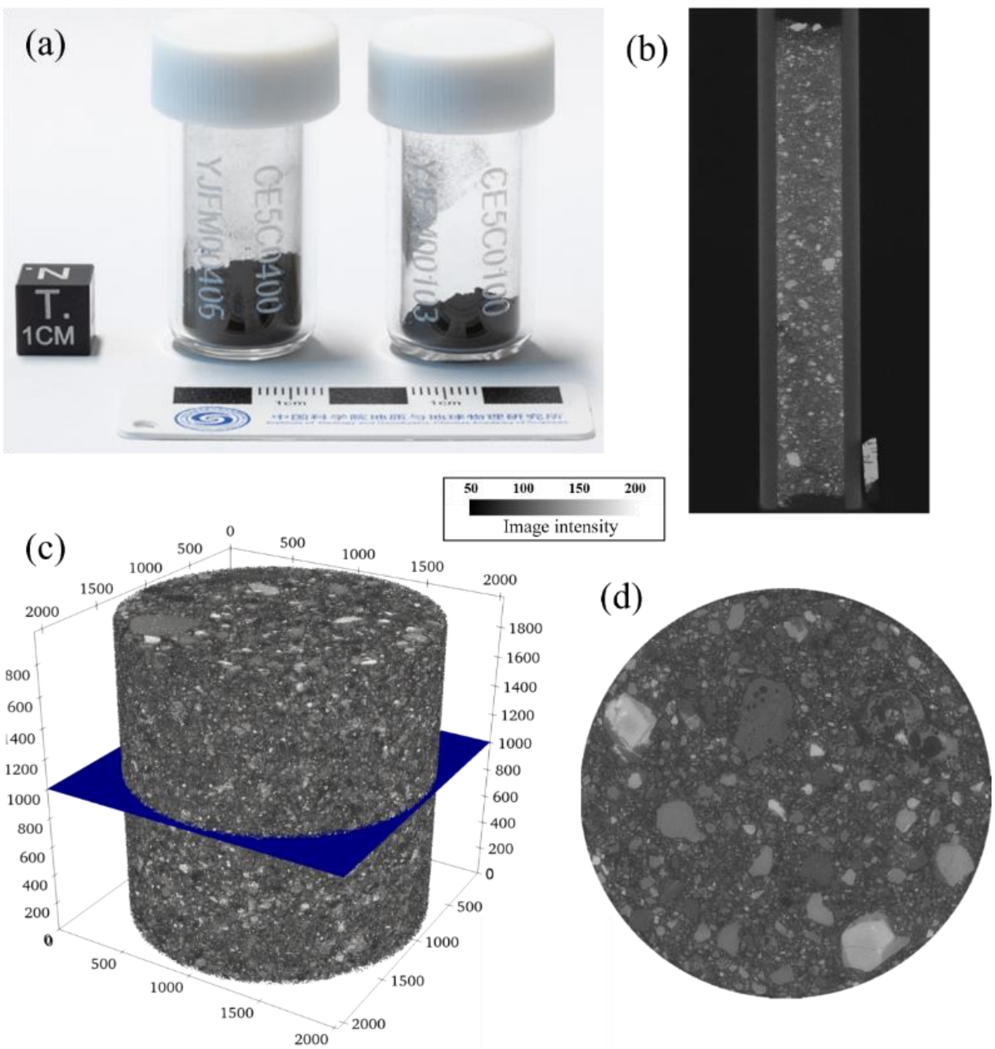

Figure 1. The CE-5 lunar regolith samples and micro-CT scans. (a) Lunar regolith samples CE5C0100YJFM00103 and CE5C0400YJFM00406 allocated to the Institute of Geology and Geophysics, Chinese Academy of Sciences. (b) A 2D scan at a resolution of 2.20 μm of the tube as an overview of the sample. (c) Reconstructed grayscale volume of the sample. (d) An example horizontal slice of the sample corresponding to the middle plane in (c).

2.2 Machine Learning-based Image Segmentation

Accurate segmentation of the lunar regolith particles is crucial to extracting information from the micro-CT images. Traditional methods could segment raw images into different components, such as simple thresholding (Otsu, 1979) and marker-controlled watershed algorithms (Meyer & Beucher, 1990). However, these methods may encounter challenges due to the complexity of mineral composition and intricate surface morphologies of lunar regolith particles, leading to both over-segmentation and under-segmentation. We employed a machine learning-based segmentation method to address this problem. There are two main steps involved in the 3D segmentation of lunar regolith particles: a primary voxel-wise classification that identifies different phases in the images including solids and voids, and a secondary segmentation that isolates the individual particles based on boundaries.

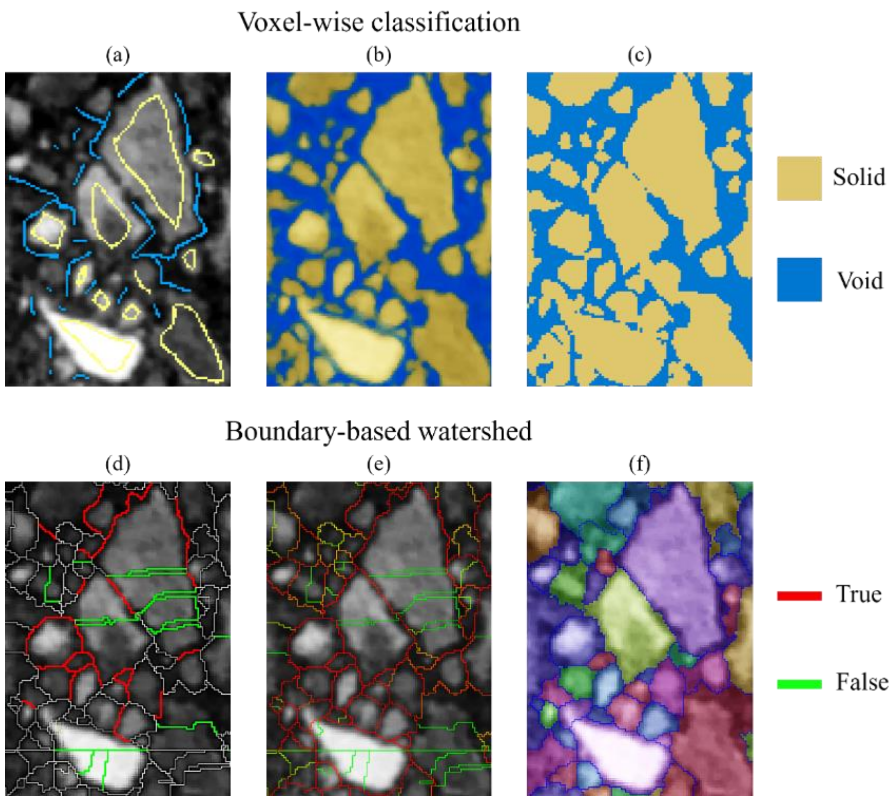

Figure 2. Examples of voxel-wise classification and boundary-based watershed. (a) Manually annotated micro-CT slice. (b) Probability map of voxel classification. (c) Voxel-wise classification results. (d) Predicted boundaries based on distance transform and annotations on good or bad boundaries. (e) Probability map of particle boundaries. (f) Boundary-based watershed segmentation results.

The random forest algorithm presents several advantages for image segmentation applications (Breiman, 2001; Shotton et al., 2008). It is effective in managing high-dimensional data and demonstrates robustness to noise and outliers. By evaluating feature importance, this method facilitates the selection of the most relevant features. Additionally, random forest reduces overfitting and manages complex boundaries with precision. Its computational efficiency is advantageous for large datasets, and its ability to integrate diverse information types, including shape and texture, makes it particularly suitable for processing 3D micro-CT scans of lunar regolith samples.

A voxel-wise random forest classifier was employed to segment the volume data into solids (i.e., distinguishable particles with sizes larger than micro-CT resolution) and voids, considering multiple features, including intensity, boundaries and texture (Sommer et al., 2011). Arbitrarily chosen voxels were manually labeled in 2D slices according to their phase-contrast features, serving as the training set to train the random forest classifier (Figure 2a). The classifier was able to estimate the probability that a voxel belongs to each semantic class (Figure 2b). Then, a probability threshold was applied to the entire 3D volume to generate voxel-wise classification results (Figure 2c). To ensure optimal accuracy, the model was iteratively updated by adding more voxel labels until satisfactory segmentation was achieved throughout the volume.

The primary segmentation could distinguish between different phases. However, the boundaries among particles typically appear to be classified as the solid phase due to the partial volume effect that is related to the limited resolution. Thus, a boundary-based watershed algorithm (Andres et al., 2011) was used to further segment the contacting assembly into isolated particles. The potential 3D boundaries (grey edges in Figure 2d) were generated by the watershed algorithm based on the distance transform. By training the random forest classifier using manually annotated true boundaries (in red) and false boundaries (in green) (Figure 2d), a boundary probability map (Figure 2e) was generated. The packed lunar regolith particles could be separated into distinct 3D regions with labels by applying a probability threshold (Figure 2 & Figure 3). With this two-step image processing, the lunar regolith particles could be segmented from micro-CT images, allowing for the creation of a comprehensive database containing massive information.

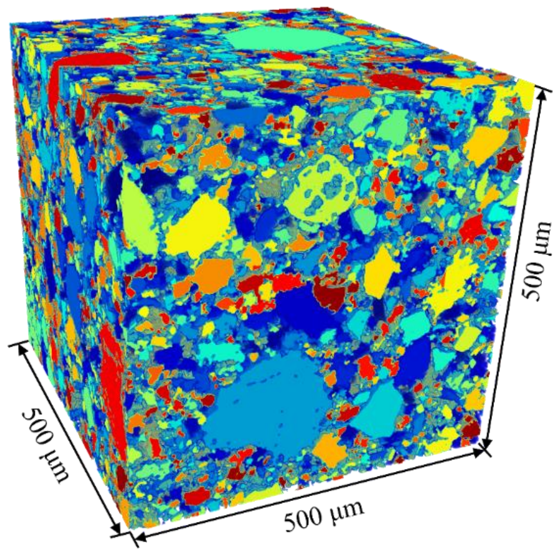

Figure 3. An example of the 3D segmentation. The region (500 μm × 500 μm × 500 μm) is cropped from the entire volume with randomly assigned pseudo-color labels for visualization.

2.3 Density Calibration

Prior studies have measured the bulk density and true density of CE-5 lunar regolith samples through the helium displacement method (Li et al., 2022). However, a significant gap remains regarding the spatial density distribution within lunar regolith particles. Micro-CT imaging has emerged to interpret the density distribution within scanned samples by utilizing the correlation between grayscale image intensities and material densities (Humbert et al., 2016; Sudhyadhom, 2020). Voxel intensities of 3D micro-CT scans reflect the degree of X-ray attenuation, which is affected by several factors including the X-ray energy spectrum, scan parameters, and material properties. However, it is important to note that the primary influence on voxel intensities should be the material properties alone when using the same micro-CT machine and conducting a single scan. The voxel intensity is directly proportional to the linear attenuation coefficient μ of the material in the corresponding spatial range, which is a product of the mass attenuation coefficient μ_{m} and the material density ρ:

$$\mu = \rho \times \mu_{\mathrm{m}}, \tag{1}$$

where the mass attenuation coefficient μ_{m} influenced by the photoelectric effect and Compton scattering, both of which are controlled by multiple variables such as atomic number and photon energy:

$$\mu = \tau + \sigma \approx \alpha Z^{4.5} E^{-3} + \beta Z E^{-1}, \tag{2}$$

where Z is atomic number, E is photon energy, and α, β are two constants. The equations above demonstrate a monotonic nonlinear relationship between voxel intensities and material densities, which illustrates that dense materials could attenuate more X-rays and result in higher voxel intensities. Therefore, it is appropriate to inversely estimate the spatial density distribution of the lunar regolith sample by means of X-ray micro-CT imaging.

To quantitatively correlate voxel intensities and material densities, several phases including air and crystalized minerals with known densities were selected as references for the calibration, which were carefully confirmed to be free from artifacts or other distortions that may introduce inaccuracies (Figure 4a). By performing polynomial interpolation between discrete data points of extracted voxel intensities from these referencing regions and their densities, the non-linear relationship was established (Figure 4b):

$$\rho = 0.0014 I^3 - 0.6868 I^2 + 124.59 I - 3897, \tag{3}$$

where ρ is the estimated material density, I is the intensity of the corresponding voxel in micro-CT images.

Equation (3) was then applied to convert voxel intensities into material densities, providing a spatial density distribution throughout the entire reconstructed volume, thus enabling the density assessment and mineral identification within the scanned region.

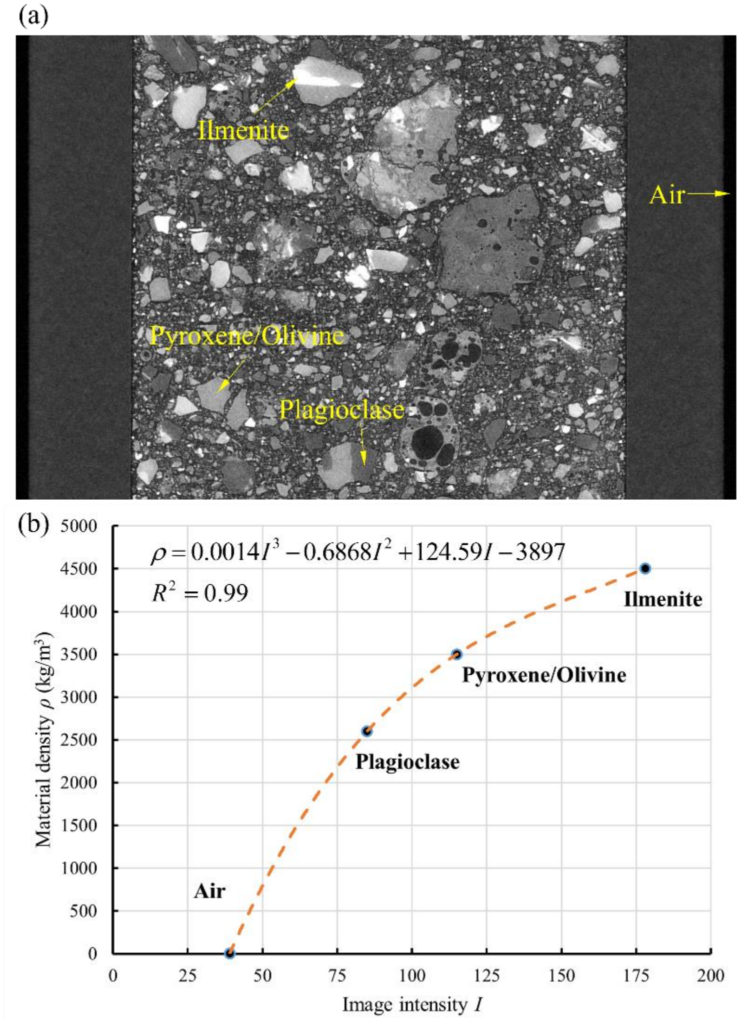

Figure 4. Calibration of material density based on micro-CT image intensities. (a) Phase mapping in a micro-CT slice. Four types of materials were distinguished based on phase-contrast features. (b) Fitted calibration curve of material densities and voxel intensities.

2.4 Quantification of Particle Shape Characteristics

The shape characteristics of lunar regolith particles are crucial for understanding the geological processes that have shaped the Moon's surface. Furthermore, it is essential to characterize and quantify the shape parameters of lunar regolith particles in order to predict their behavior in engineering applications, such as serving as foundation soils capable of bearing building loads and as potential materials for lunar base construction.

Lunar regolith particles acquire their irregular shapes as a result of constant bombardment by meteoroids and micrometeoroids during long-term space weathering (Zhang et al., 2023). These particles could be found in various forms, such as angular fragments, elongated shards, or agglutinates. In contrast to terrestrial soils which tend to have round shapes, the lunar regolith particles retain its sharp edges and angular characteristics since weathering and erosion processes on the Earth are absent on the Moon.

The spherical harmonic (SH) analysis is used to describe and measure the multiscale shape characteristics of particles (Garboczi, 2002; Shen et al., 2009; Zhou et al., 2015; Wei, 2018; Chen et al., 2021). SH functions can be employed to represent the surfaces of particles obtained from micro-CT images:

$$r(\theta,\varphi)=\sum_{n=0}^{\infty}\sum_{m=-n}^{n}c_n^m Y_n^m(\theta,\varphi)\,, \tag{4}$$

$$Y_n^m(\theta,\varphi)=\sqrt{\frac{(2n+1)(n-m)!}{4\pi(n+m)!}}P_n^m(\cos\theta)e^{im\varphi}\,, \tag{5}$$

where $r(\theta,\varphi)=\sqrt{\sum_{x,y,z}(\kappa-\kappa_0)^2}$ is the polar radius from particle centroid with spherical coordinates $\theta\in[0,\pi]$ and $\varphi\in[0,2\pi]$. n is the SH degree and m is the order and c_n^m is the corresponding SH coefficient. $P_n^m(\cos\theta)$ denotes the Legendre function of SH degree n and order m, which could be expressed by Rodrigues's formula:

$$P_n^m(x)=(1-x^2)^{|m|/2}\cdot\frac{d^{|m|}}{dx^{|m|}}\left[\frac{1}{2^n n!}\cdot\frac{d^n}{dx^n}(x^2-1)^n\right]. \tag{6}$$

By inputting the polar coordinates matrix of the discrete points on the particle surface into equation (4), the spherical coefficients c_n^m could be obtained by solving the linear equation system using the standard least squares estimation method. The modulus of c_n^m at different spherical harmonics degree n can be calculated as follows:

$$L_n=\sqrt{\sum_{m=-n}^{n}\|c_n^m\|^2}\,. \tag{7}$$

The spherical harmonics describe the morphological features of the particle shape at different scales. A higher SH degree n allows for more detailed characterization and a more accurate reconstruction of the particle surface geometry. In this study, we adopted a maximum SH degree of 25 to analyze the multi-scale shape features of lunar regolith particles. The SH coefficients L_0 represents the particle volume and L_1 does not affect the particle morphology, L_2 to L_4 reflect the general shape, L_5 to L_8 depict the local roundness, while L_9 and above capture the surface texture at a fine-scale level. To quantify the morphological complexity at different spherical harmonic degrees, the spherical harmonic descriptors D_n are proposed as follows:

$$D_n = \frac{L_n}{L_0}, (n = 2, 3, 4), \tag{8}$$

where all the L_n were divided by L_0 to remove the effect of particle volume. Furthermore, L_1 was not taken into consideration because it does not influence the reconstructed morphology of the particle using spherical harmonics.

Generally, the exponential relation between the spherical harmonic descriptor D_n and the spherical harmonic degree n can be expressed by:

$$D_n \propto n^{\beta}, \tag{9}$$

where β is the slope of the fitted line for $\log(D_n)$ versus $\log(n)$. Equation (9) reflects the self-similarity of the particle shape, which can be quantified by the fractal dimension FD (Xie, 2020). FD is positively correlated with the complexity, roughness, or irregularity of the surface geometry. It could be calculated by the following expression (Russ, 2013; Wei et al., 2018):

$$FD = \frac{6 + \beta}{2}. \tag{10}$$

Form factors are also extensively used to quantify the overall shape characteristics of terrestrial and non-terrestrial bodies (Zhao & Wang, 2015; Zhu & Zhao, 2021; Deitrick & Cannon, 2022; Nie et al., 2023). The most widely used form factors include elongation index (EI), flatness index (FI) and aspect ratio (AR) which are denoted as:

$$EI = \frac{I}{L}, \tag{11}$$

$$FI = \frac{S}{I}, \tag{12}$$

$$AR = \frac{S}{L}, \tag{13}$$

where L, I and S are the largest, intermediate and shortest dimensions of particles obtained from a bounding box estimation, which is dependent on the order of measurement (Fujiwara et al., 1978; Katagiri et al., 2015; Michikami et al., 2018; Tsuchiyama et al., 2022). To facilitate the comparison with previous measurements, the bottom-up method (La Spina & Paolicchi, 1996) is adopted to measure the three dimensions in the order of S, I and L, which is consistent with Tsuchiyama et al. (2022). According to the classification criteria of Zingg (1935), particles become more elongated as EI decreases and more platy as FI decreases. Conversely, as AR increases, particles become more spherical (Figure 12).

3 Results

3.1 Reconstruction and Segmentation of Micro-CT Images

The digital volume of interest is composed of 2,000 slices of 2025 × 2070 grayscale images, discretizing the samples into approximately 8,383 million voxels. With the application of machine learning-based image processing methods, the labelled grayscale volume of 710,226 lunar regolith particles were obtained (Figure 5), allowing for the observation and characterization of the individual particle structure. The segmentation results demonstrate the effectiveness of the proposed methods in accurately separating packed lunar regolith particles in micro-CT images. The segmented regions were labeled sequentially, enabling the volume extraction of any arbitrary particle through traversal. A database was established to store, organize, and manage the data of these particles. It is the first database with high-resolution micro-CT images of such a large number of lunar regolith particles. This database helps extract grain-scale information of the CE-5 samples and provides a comprehensive understanding of the properties of lunar regolith.

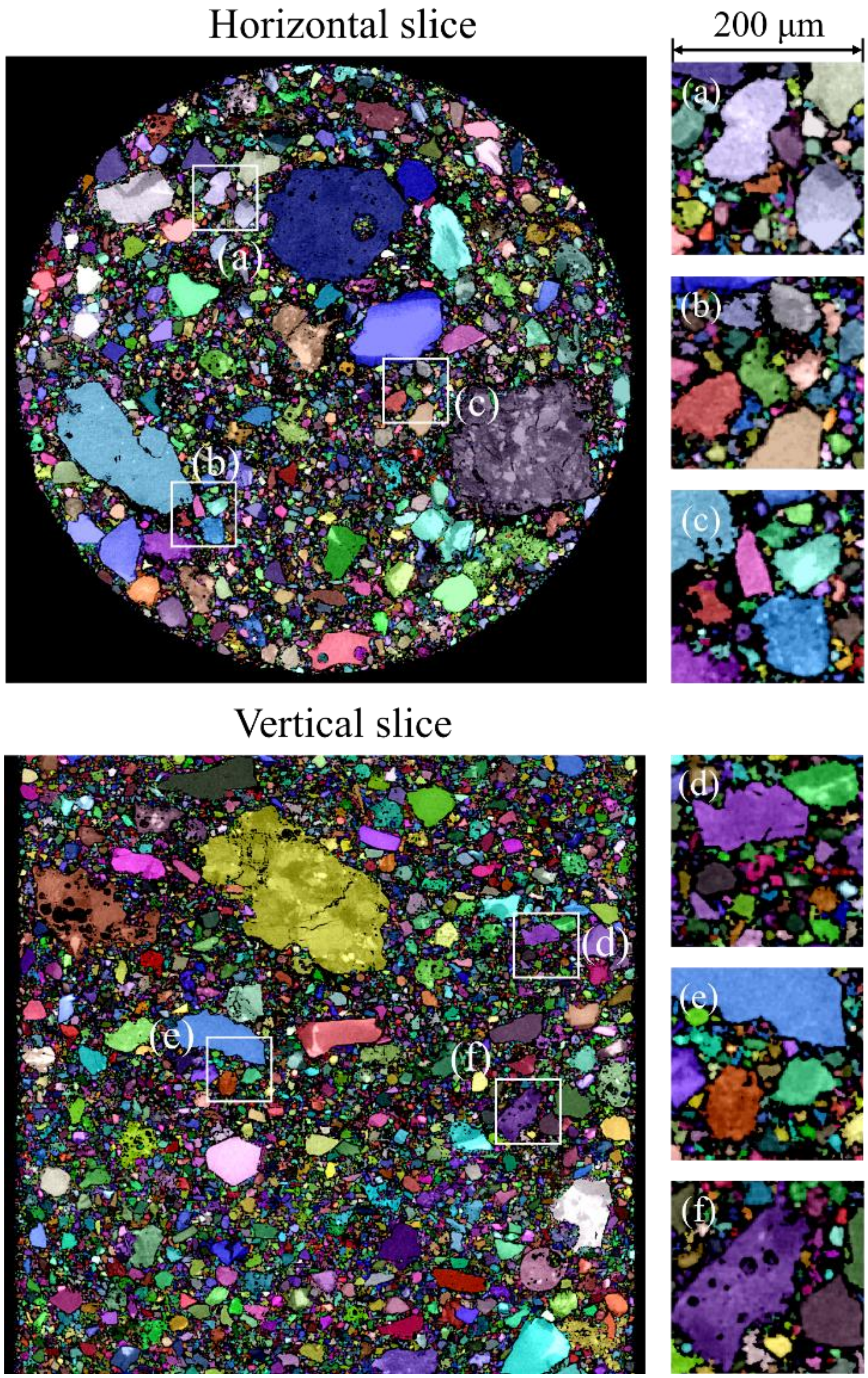

Figure 5. Example segmented lunar regolith particles in horizontal and vertical slices of micro-CT scans. Randomly assigned pseudo-color labels of individual lunar regolith particles are superimposed transparently on the grayscale image for illustration of the segmentation results.

To quantitatively evaluate the accuracy of our segmentation methods, manual inspections were performed on the machine learning-based segmentation results. For example, we found 29 inaccurate segmentations in Figure 5 (a-f) from 371 segmented particles mostly on small particles that suffer from the partial volume effect. This shows that the accuracy of our machine-learning based segmentation is around 92.2%, with almost perfect segmentation performance for large particles.

3.2 Particle Size Distribution

Particle size distribution is a fundamental physical property of lunar regolith that significantly influences its mechanical and thermal behaviors. To obtain the particle size distribution of the CE-5 samples, we calculated the equivalent diameters of all the 710,226 particles segmented from the micro-CT images. The particle size distribution obtained by image segmentation (Figure 6a) revealed that the size of CE-5 lunar regolith particles ranges from fine dust (<5 μm) to large fragments (>100 μm) with a median particle size of 57.5 μm (Figure 6a), which is smaller than Apollo 11 (mature/submature), Apollo 16 (mature), and Luna 24 (immature) samples. Several lunar regolith particles at different sizes are shown in Figure 6b as examples, further illustrating the dispersed size of lunar regolith particles. In geotechnical terms, the CE-5 lunar regolith sample could be classified as sandy silt or silty sand.

3.3 Density Estimation and Mineral Characterization

The correlation between material densities and voxel intensities is established based on the introduced calibration methods, providing the estimated density distribution of the digital volume (Figure 7a). The spatial density distribution could be used to characterize and identify minerals in lunar regolith particles. The lunar soil particles from the CE-5 mission can be broadly categorized into the following types based on the classification criteria of Heiken et al. (1991) and Katagiri et al. (2015): irregular agglutinate particles with internal vesicles, polymineralic particles and monomineralic particles (Figure 7c). For instance, Figure 7b provides a detailed view of a fragmented polymineralic particle with parallel veins, showing the presence of four phases with distinct densities. The alternating phases with vein-like pattern can be inferred as pyroxene-ilmenite pair, which is a typical indicator of shock compression related to an impact event (Tomioka & Fujino, 1997). Based on the estimated density distribution (Figure 7d) and the range of densities of known minerals, these four phases could be identified as ilmenite, pyroxene, plagioclase, and fractures.

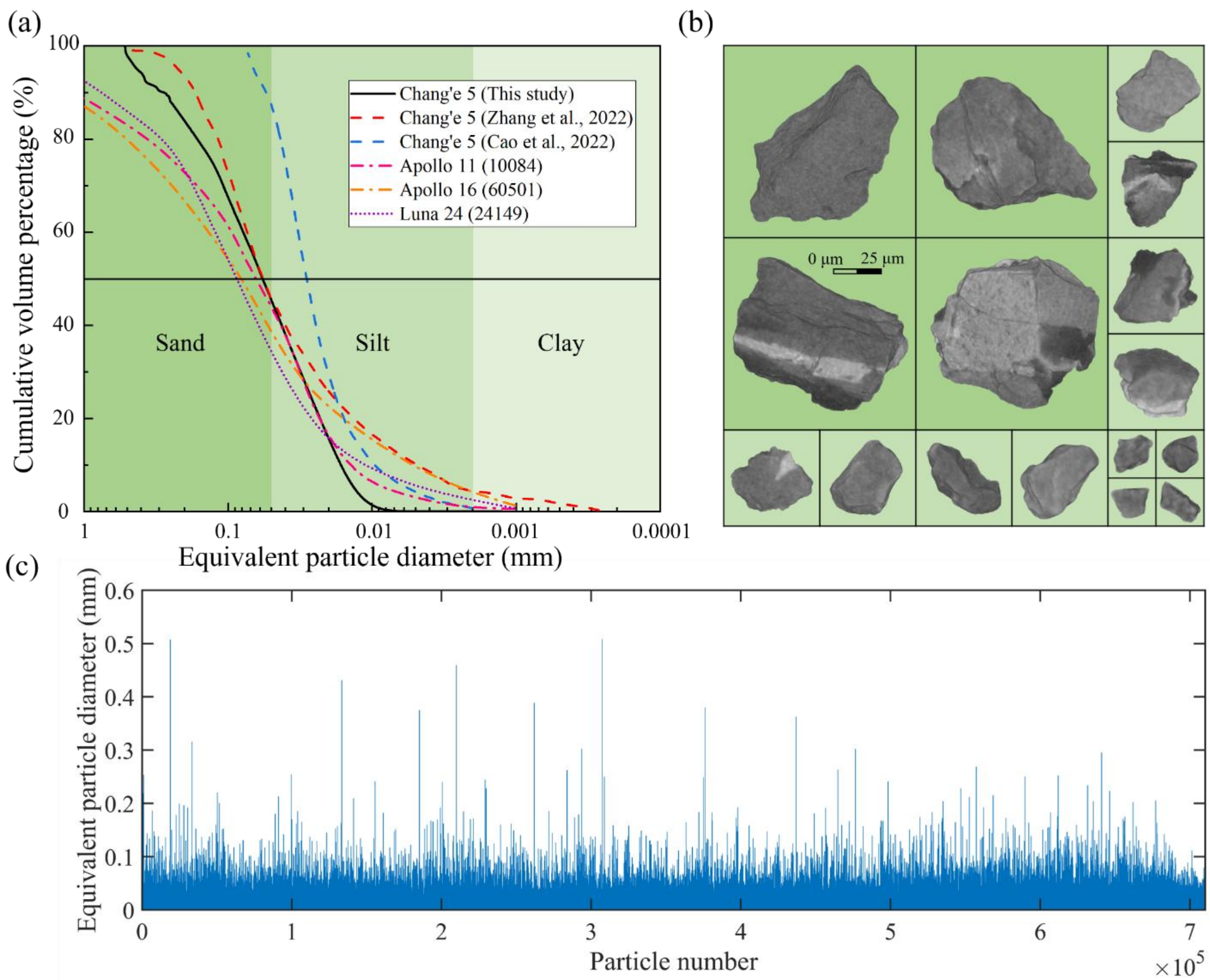

Figure 6. Particle size distribution of the CE-5 lunar regolith sample and representative particles with different sizes. (a) The cumulative volume distribution versus equivalent particle diameter of the CE-5 lunar regolith sample determined by our micro-CT imaging technique and other different methods (Cao et al., 2022; Zhang et al., 2022). The particle size distributions of Apollo 11, Apollo 16 and Luna 24 (Graf, 1993) are also presented for comparison. (b) The grayscale reconstructed volume of segmented particles with different particle sizes. (c) The equivalent particle diameter for all 710,226 particles extracted from micro-CT images.

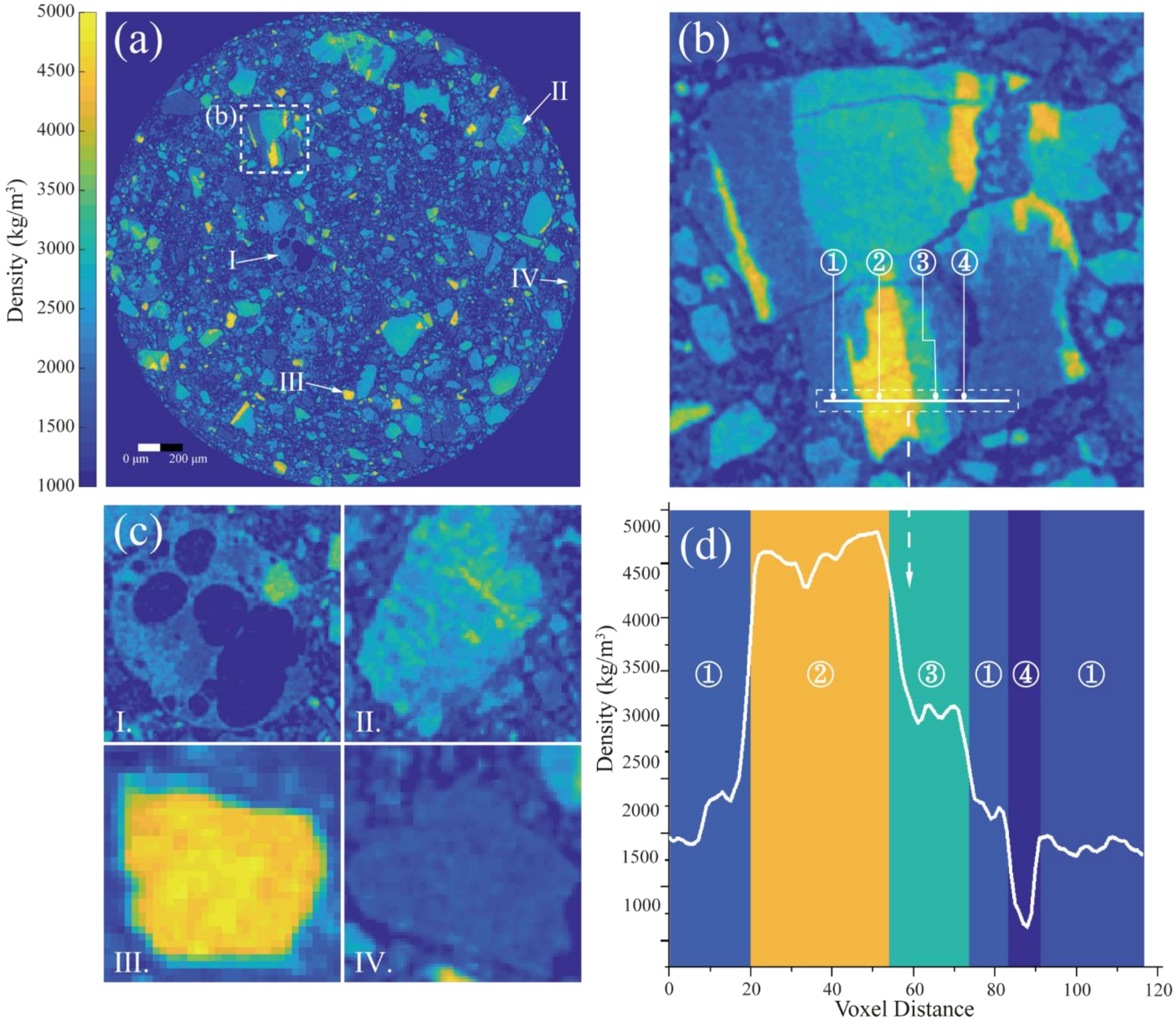

Figure 7. Density calibration and mineral phase identification based on micro-CT images. (a) Estimated density distribution in a micro-CT slice. (b) Phase-contrast induced features in detail zoomed from (a). (c) Representative lunar regolith particles with distinguished types of mineralogical textures including agglutinate (I), polymineralic (II) and monomineralic (III & IV) particles. (d) The profile of estimated density along the white line in (b).

The density distribution can also contribute to revealing the 3D microstructural features of lunar regolith particles in the CE-5 sample. By thresholding the estimated density distribution, phase-induced features could be extracted. Figure 8a, Figure 8b and Figure 8c present the 3D structure of a polymineralic particle with an ilmenite vein, an agglutinate particle with several isolated vesicles and a fragmented breccia particle, respectively.

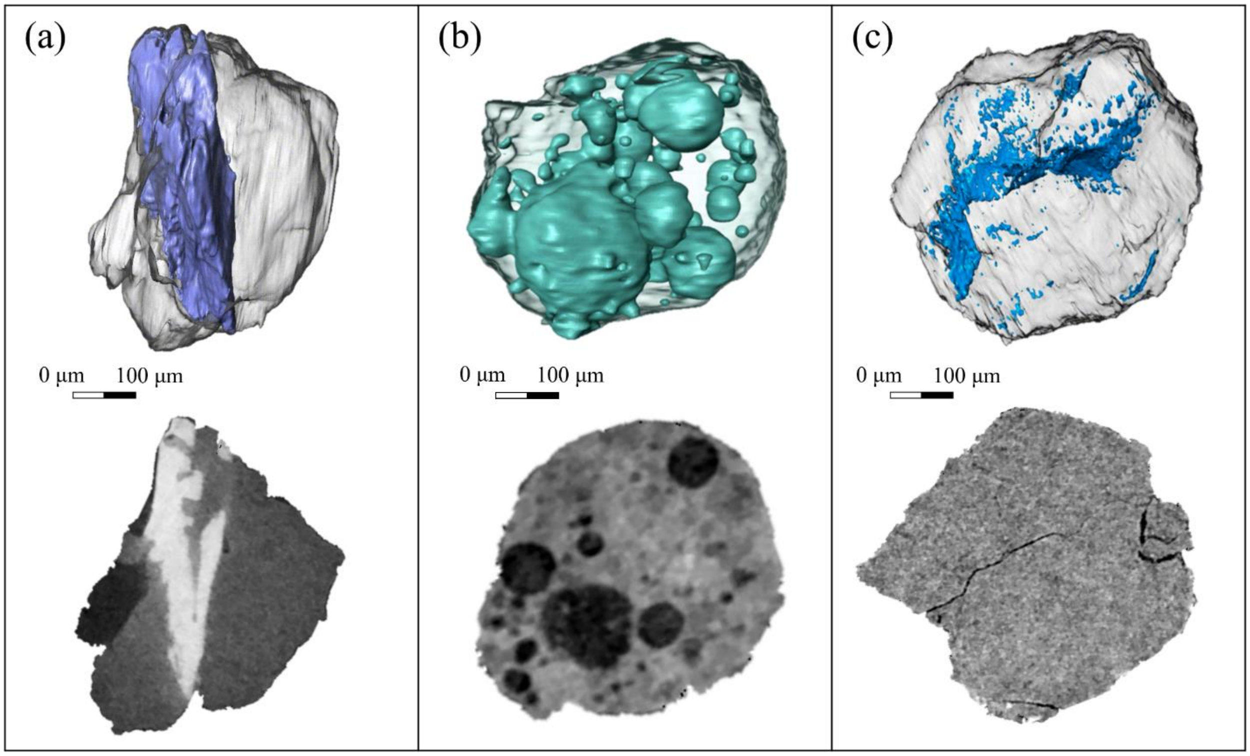

Figure 8. 3D structures of three typical lunar regolith particles and representative micro-CT slices. (a) A polymineralic particle with high-density ilmenite (in purple). (b) An impact glass particle with isolated vesicles (in green). (c) A breccia particle with fractures (in blue).

The spatial density distribution derived from micro-CT images enabled the density estimation of individual lunar regolith particles (Figure 9a), allowing for further evaluation of both bulk density (1.58 g/cm^3) and true density (3.17 g/cm^3) of the CE-5 sample. It should be noted that bulk density refers to the mass of the lunar regolith per unit volume, including both the particles and the voids, and true density refers to the mass of the lunar regolith per unit volume of the solids alone, excluding both internal pores within the particles and external voids between them. These measurements align with the density values obtained through laboratory measurements (Zhang et al., 2022), indicating the accuracy of our methods.

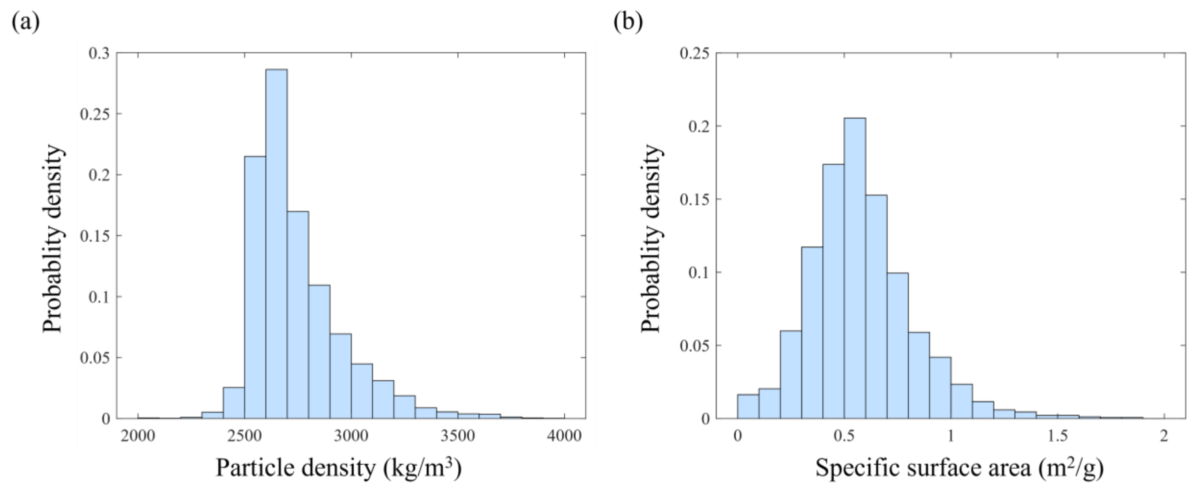

Figure 9. Probability density distribution of properties of lunar regolith particles segmented from micro-CT images. (a) Histogram of particle density. (b) Histogram of specific surface area.

Based on the known types of minerals and the range of mineral densities (Tian et al., 2021), the mineral content (wt.%) of the CE-5 samples can be assessed by thresholding the estimated density distribution (Table 1). It should be noted that some minerals with similar densities were combined as one category. The overall assessment of mineralogy is consistent with previous measurements (Li et al., 2022; Zhang et al., 2022; Cao et al., 2022; Qian et al., 2023).

Table 1. Mineral content of CE-5 lunar regolith samples obtained from micro-CT imaging compared with previous laboratory measurements (Li et al., 2022; Zhang et al., 2022; Cao et al., 2022; Qian et al., 2023).

Sources	Methods	Glass/Plagioclase	Pyroxene/Olivine	Ilmenite
Li et al. (2022)	XRD	46.7%	47.7%	4.5%
Zhang et al. (2022)	XRD	45.9%	48.1%	6.0%
Cao et al. (2022)	Raman	49.7%	42.3%	3.3%
Qian et al. (2023)	Raman	38.9%	55.9%	5.2%
Our study	Micro-CT	45.6%	49.7%	4.7%

3.4 Shape Characteristics of Lunar Regolith Particles

To quantify the shape characteristics of lunar regolith particles and minimize errors introduced by voxelization, spherical harmonics and form ratios were computed for 20,396 particles which have volume larger than 15,000 voxels, which is approximately equivalent to the shortest dimension of 20 μm. The triangular surface meshes of the particles were generated and saved in .STL files (Figure 10a) using the open-source code iso2mesh (Fang & Boas, 2009).

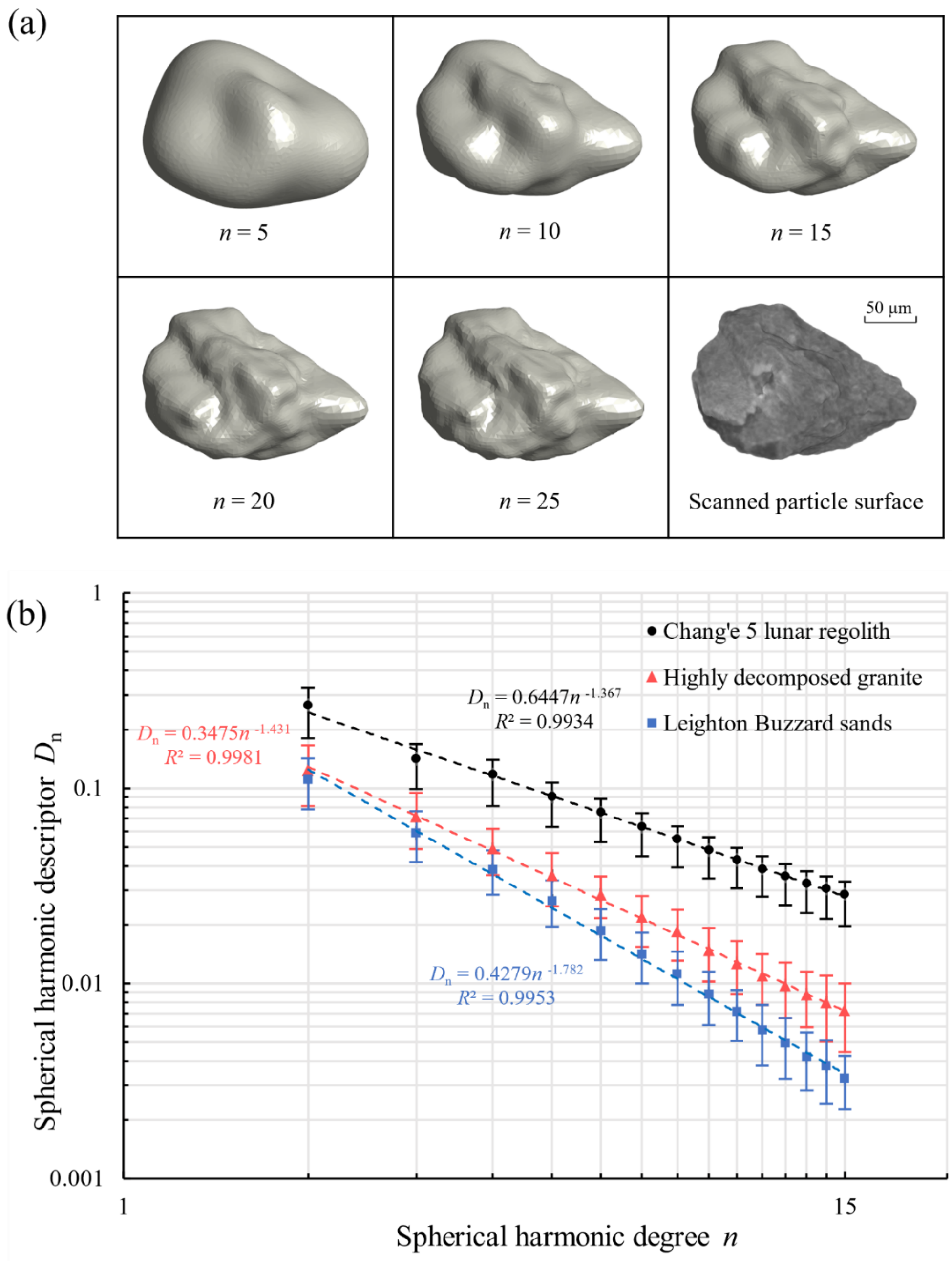

Figure 10. Spherical harmonic analysis of CE-5 lunar regolith particles. (a) Comparison between scanned particle surface and reconstructed particle surface with different degrees of spherical harmonics (n from 5 to 25). (b) Spherical harmonic descriptors as a function of the spherical harmonic degree n for CE-5 lunar regolith particles and two types of terrestrial soils. Data of Leighton Buzzard sand (LBS) and highly decomposed granite (HDG) are from Wei et al. (2018).

Spherical harmonic analysis was conducted with a maximum SH degree of 25. It was found that a satisfactory reconstruction could be achieved when the SH degree $n > 15$ by comparing the reconstructed particle shapes at different spherical harmonic (SH) degrees with the actual particle shape (Figure 10a). The statistical analysis (Figure 10b) reveals a linear correlation between the mean spherical harmonic descriptors and the spherical harmonic degree in log-log scales (Figure 10b), demonstrating the self-similarity of multiscale morphological features of lunar regolith particles. Our results indicate that CE-5 particles exhibit the highest spherical harmonic descriptors among the three types of particles. According to equation (14), linear fitting was performed for $\log(D_n)$ versus $\log(n)$ of three types of particles (Figure 10b). Based on the fitting parameters, the mean fractal dimension FD of CE-5, HDG and LBS particles were calculated to be 2.32, 2.28, and 2.11, respectively. The reconstruction of the particle surface also allows for the estimation of the specific surface area of each lunar regolith particle (Figure 9b). The mean value of the specific surface area is found to be 0.59 m^2/g, which is close to the previous result (0.56 m^2/g) from Li et al. (2022).

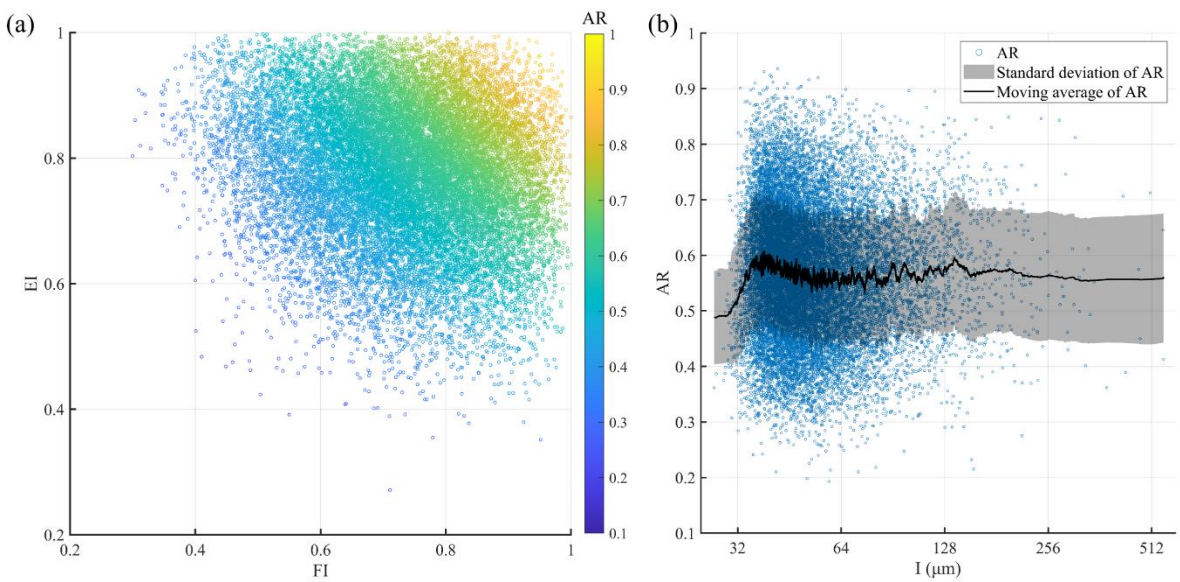

Figure 11. Form factors distributions of CE-5 lunar regolith particles. (a) Zingg diagrams of CE-5 lunar regolith particles displaying distribution of EI, FI, and aspect ratios (AR). (b) The relationship between AR and the intermediate length (I) revealing size dependency of particle shape. The moving average of AR is plotted with shaded error bars indicating the standard deviation.

The form factors of the 20,396 lunar soil particles are shown in Figure 11a. The mean elongation index (EI), flatness index (FI), and aspect ratio (AR) were found to be 0.7322, 0.7786, and 0.5679, respectively. Size dependency was observed by calculating the moving average of AR as a function of the intermediate particle length (I), which serves as a representative measure of particle size. The AR initially increases and reaches a peak at approximately 40 μm, after which it declines with observable fluctuations around the mean value (Figure 11b). Considering that the form factor is size-dependent, the CE-5 samples were divided into four particle size groups for comparison with Luna and Apollo samples (Tsuchiyama et al., 2022). The mean form factors are shown as Zingg diagrams (Figure 12), where EI is plotted against FI . Our results demonstrate that data points of CE-5 are further left and lower in the diagram compared to other samples regardless of particle size, indicating a smaller aspect ratio and a less spherical shape.

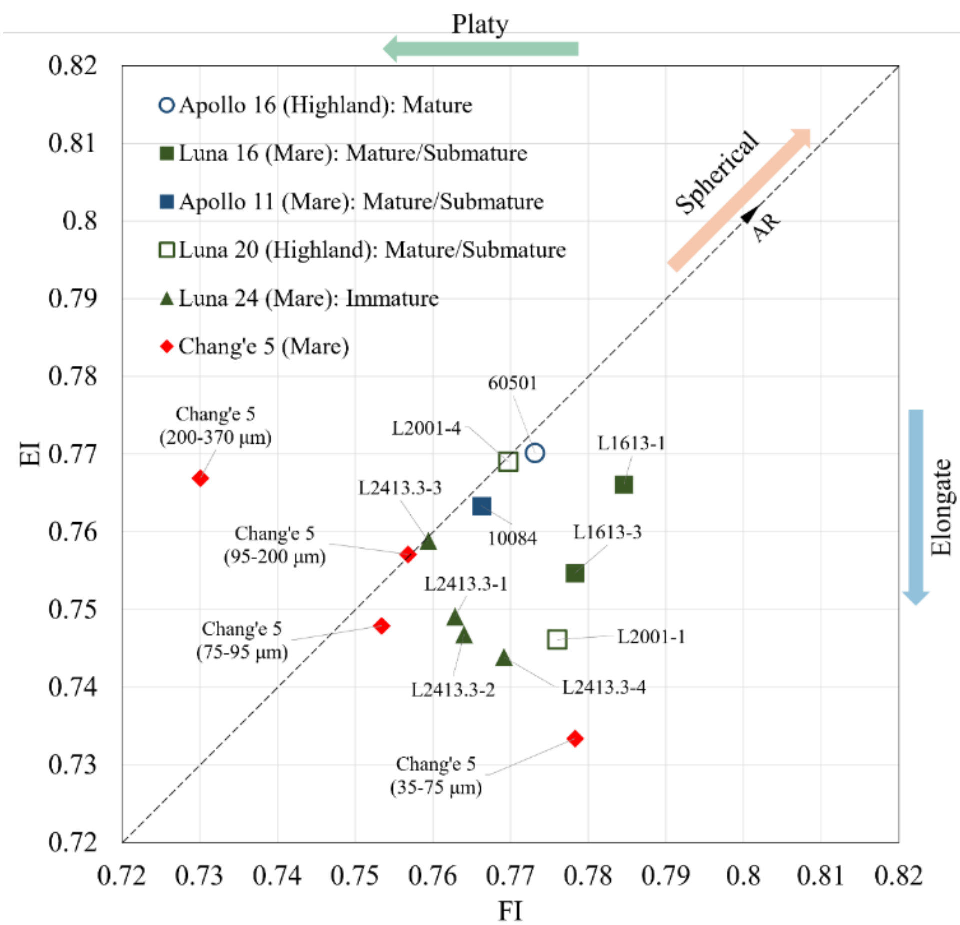

Figure 12. Zingg diagrams showing the mean form factors of CE-5 lunar regolith particles and comparison with Luna and Apollo missions.

4 Discussion

In this study, we quantitatively evaluated several critical physical properties of CE-5 lunar regolith samples using micro-CT imaging. Our results generally agree with previous studies with slight differences possibly due to differences among different batches of samples and varying measurement methods. The blue and red dashed curves in Figure 6a represent the measurements of Cao et al. (2022) using Raman particle analysis and Zhang et al. (2022) using laser diffraction respectively. The obtained median particle size in our study is 57.5 μm, close to 55.24 μm from Zhang et al. (2022) and larger than 28.4 μm from Cao et al. (2022). We also found that particles smaller than 10 μm accounted for only 1.4% of the total volume in our segmentation. However, Zhang et al. (2022) and Cao et al. (2022) reported volume fractions of approximately 17.0% and 10.8% for particles under 10 μm, respectively. This is attributed to the limited spatial resolution of micro-CT images, which poses challenges in accurately identifying very fine particles. The median particle size would be 73.6 μm for Zhang et al. (2022) and 30.7 μm for Cao et al. (2022) with a cutoff particle size of 10 μm.

The obtained median particle size of the CE-5 samples is smaller than that of Apollo 11, Apollo 16 and Luna 24 samples (Hapke, 1968; Duke et al., 1970; Carrier III, 1973; Graf, 1993). The particle size distribution is widely used to quantify the maturity of lunar regolith samples. Generally, a smaller median particle size is associated with a higher degree of maturity (Chen et al., 2023; Li et al., 2022; Zhang et al., 2021). However, the immature lunar soil samples from the Luna 24 mission exhibit a larger median grain size compared to the mature samples from Apollo 11 and Apollo 16. This counterexample indicates that median grain size alone is insufficient to determine the maturity of lunar regolith samples. The particle size of lunar regolith might not monotonically correlated with maturity as the space weathering effect on the particle size was controlled by the competing effects of micrometeorite comminution and agglutination (McKay et al., 1974). Moreover, the particle size of lunar regolith is significantly determined by the intrinsic crystal size of the protolith, which is influenced by the cooling rate and the chemical composition of the magma (Head & Wilson, 2020; Qian et al., 2024). He et al. (2022) suggests that CE-5 basalts may experience rapid cooling after eruption, which may explain the relatively small particle size of CE-5 samples.

The assessment of mineral content in our study is consistent with previous research using X-ray diffraction (XRD) (Zhang et al., 2022; Li et al., 2022), which is a mature technique for identifying crystalline phases and quantifying their abundance. However, XRD relies on the identification of each phase, which may not always be trivial. For example, XRD is unsuitable for amorphous materials (e.g., glass) and trace amount phases (<0.1–1.0%) may be undetected (McCusker et al., 1999). In addition, quantitative analysis of minerals content is inferred from XRD patterns instead of direct measurement. Our study relies on the 3D volumetric representation of the particles and the correlation between density and the level of X-ray attenuation in materials. This provides a non-destructive and direct measurement approach to evaluate the mineral content of lunar regolith samples with digital images. Although minerals of similar densities (i.e., glass/plagioclase and pyroxene/olivine) can hardly be distinguished, and the accurate mineral composition (e.g., EnFsWo in pyroxene) cannot be assessed by micro-CT images, the combined proportions of glass/plagioclase and pyroxene/olivine, as well as the proportion of ilmenite, still provide valuable verification for measurements from other techniques. In addition, the spatial relations between different minerals and their morphological characteristics may also aid in identifying mineral phases.

Visualization and characterization on specific particles in the CE-5 samples could provide us with a massive amount of information about the geologic history of the sampling sites. Based on micro-CT images of CE-5 samples, we identified agglutinate particles, polymineralic particles and monomineralic particles which are classified by Heiken et al. (1991) and Katagiri et al. (2015). This finding demonstrates that the CE-5 sample exhibits considerable similarity to other lunar regolith samples in terms of mineralogical textures. Li et al. (2021) and Qian et al. (2024) proposed that the agglutinate abundance (~16.6%) in CE-5 soil is lower than that observed in all Apollo mature soils (>30%), which may indicate the immaturity based on the established correlation between agglutinate abundance and soil maturity.

The observed high-intensity phases (Figure 8a) confirmed the existence of mineral composition with high-density metal elements such as Fe and Ti. The vesicles in the glass particle (Figure 8b) may have been formed when dissolved gases bubble out of the magma as it decompresses during its approach to the surface and lava solidifies before the gases can escape (Blatt et al., 2006; Yang et al., 2022). It may imply past high-temperature events such as meteorite impacts. The fragmentation of lunar regolith particles (Figure 8c) could be induced by several stress-related processes in many ways, including temperature change, application and release of overburden pressure, shearing forces, crystal growth, water pressure or tension (Steiglitz, 1988).

In order to compare the shape characteristics of lunar regolith particles and terrestrial geomaterials, the spherical harmonics data of Leighton Buzzard sand (LBS) and highly decomposed granite (HDG) sourced from Wei et al. (2018) are also included in Figure 10b. The LBS have rounded and smooth particle surfaces because of geological transportation processes while the HDG are typically angular, rough, and have numerous surface asperities. Our results suggest that lunar regolith particles exhibit the largest spherical harmonic descriptors D_n among three types of geomaterials, while HDG displays larger spherical harmonic descriptors than LBS. This result indicates that lunar regolith particles exhibit more complex morphological features with more angular shapes, sharper edges and finer textures compared with LBS and HDG (Figure 10b). The spherical harmonic descriptors D_n shifts from capturing the overall shape to detailing surface roughness as the SH degree n increases. The fractal dimension FD which is calculated from the slope of $\log(D_n)$ versus $\log(n)$ describes the complexity and self-similarity of particle shapes. A low FD indicates that the particle shape is relatively smooth and less textured. It also suggests a low self-similarity, which means the particle surface does not have the same level of fine structural details or variations seen in particles with higher fractal dimensions. The particle shape of sandy soils and sedimentary deposits on Earth are primarily influenced by several geomorphological processes that involves various physical, chemical, and biological mechanisms over an extended period of time (Crook, 1968; Hiebert & Bennett, 1992). For instance, LBS is classified as a transported soil that mainly experienced geological transportation processes with dissolution or chemical alteration, resulting in rounded and smooth particle surface. This leads to the lowest FD among three types of particles. In contrast, the shape of HDG particles is controlled by the initial fragmentation and erosion of granite rocks over an extended period as typical residual soils, which remains sub-angular to angular and slightly rough (Wei et al., 2018). Thus, HDG has a larger FD compared to LBS. However, the space weathering on the Moon is distinct from the weathering on the Earth. Dissolution or chemical alteration of mineral composition is absent on the Moon surface. Additionally, there are no biological processes contributing to weathering on the Moon due to the absence of life. Instead, the evolution of the lunar regolith is primarily affected by micrometeorite impacts and constant radiation of the solar wind and cosmic rays and extreme temperature variation over billions of years of geological time (Anand et al., 2004; Colwell et al., 2007). Constant radiation of the solar wind and cosmic rays shape (Laczniak et al., 2021; Thompson et al., 2016) the particle morphology in nano-scale. Thus, the surface morphology of lunar regolith at the resolution of micro-CT imaging is dominant by micrometeorite impacts, which lead to fracturing, fragmentation, melting and vaporization (Gu et al., 2022; Zhang et al., 2023) and also cause mechanical abrasion (Tsuchiyama et al., 2022). Most CE-5 particles possess angular and rough shapes after a long period of space weathering as shown in Figure 5, which is evident by a higher FD compared to those of HDG and LBS.

Form factors could describe the overall shape of lunar regolith particles, regarding as another potential indicator of maturity. Michikami et al. (2018) demonstrate that fresh basalt fragments produced by hypervelocity impact experiments have a lower mean aspect ratio compared to lunar regolith particles. Our results revealed that the CE-5 particles exhibit a lower mean aspect ratio compared to other lunar samples, with a tendency towards less spherical shapes, similar immaturity to Luna 24 samples (Figure 12). The morphological evolution of lunar regolith particles is controlled by the competing effect of impact fragmentation and mechanical abrasion during long-term space weathering. Fragmentation of regolith particles occurs under intense dynamic loading (Huang et al., 2016, 2018) induced by a large meteorite striking the lunar surface with a high velocity, generating strong shock waves that cause particle crushing of lunar regolith near the impact site. In contrast, abrasion occurs under dynamic loading conditions with relatively low energy (Xiao et al., 2019), such as those produced by smaller meteorites with slower impact velocities, or shock waves that have propagated from a distant impact site. In these scenarios, the shock waves are insufficient to cause substantial fragmentation but adequate to induce frictional sliding between particles, leading to the wearing and smoothing of particle surface. Thus, the relatively low AR of CE-5 particles may not necessarily suggest that they are immature, as they might experience a significant number of high-intensity impact events, which would also lead to a lower AR. More accurate constraints on the impact-induced morphological modification of irregular shaped particles require future investigations.

The particle shape characteristics of lunar regolith have multiple influences on its overall behaviors. Granular assemblies composed of particles with smaller aspect ratios are likely to exhibit stronger fabric anisotropy, which plays a crucial role in the mechanical and thermal behavior of lunar regolith (Chen et al., 2024). Irregularly shaped particles with rough surfaces can interlock more effectively, allowing for higher interparticle friction than weathered terrestrial particles. This is closely related to the compressibility of the particles, which affects the thermal conductivity and wave velocity (Lee et al., 2017). The lunar regolith layer may have lower shear wave velocity than weathered terrestrial soils of similar composition. This is due to the Moon's gravity being only 1/6 of Earth's gravity, and the irregular shapes of lunar particles lead to larger void spaces and fewer particle contacts. Considering the influence of particle shape on the propagation of seismic waves could enhance our understanding of lunar seismic activities and the resultant ground motion (Amrouche et al., 2022; Watters et al., 2019). The morphology of particles plays a significant role in the frictional behavior of granular assemblies especially under low-stress conditions (Cho et al., 2006; Rousé et al., 2008; Cavarretta et al., 2010; Katagiri et al., 2015). This may also be important for the understanding of coseismic landslide on the Moon (Schmitt et al., 2017). Katagiri et al. (2015) proposed that an increased content of agglutinate enhances the shear strength of lunar regolith. Qian et al. (2024) demonstrate a correlation between agglutinate content and regolith maturity. These observations may suggest that different regolith maturities may be associated with varying shear strengths, potentially due to the differing levels of agglutinate present. The shape of the particles may also contribute to the lower thermal conductivity of the lunar regolith, which in turn affects the Moon's subsurface temperature (Woods-Robinson et al., 2019). Moreover, thermal conductivity is a crucial factor for future in-situ resource utilization strategies, such as the sintering of lunar regolith (Han et al., 2022).

The number of samples examined has a significant impact on revealing statistical patterns of the lunar regolith particles. Take the flatness index (FI) as an example, our analysis reveals that with the increase in particle number, the mean FI exhibits significant fluctuations (Figure 13). This variability can be attributed to the insufficient particle number, where the presence of outliers or unique particles exerts a disproportionate effect on the calculated mean values. These fluctuations diminish as the particle number increases to more than 1000, where the mean value of FI gradually stabilizes within 5% standard deviation. This trend reflects the sensitivity of shape parameters to sample size, emphasizing the need for a sufficiently large number of particles to achieve reliable and consistent statistical measures. Therefore, it is essential to determine the optimal particle number that balances the need for statistical reliability and the practical constraints of sample collection and analysis. Our findings underscore the importance of considering the number of particles in studies of lunar regolith characteristics. In this study, we use a micro-CT image segmentation method, which allows us to obtain information of a vast number of particles, ensuring that conclusions drawn about the CE-5 lunar regolith samples are based on robust and representative data.

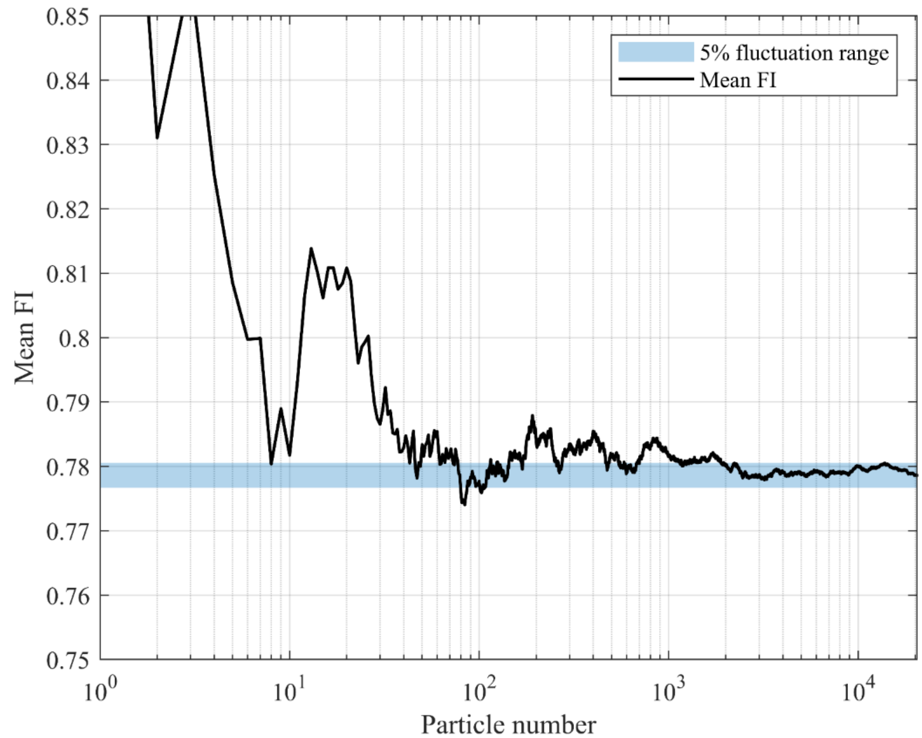

Figure 13. Influence of the total particle number on the measurement of mean flatness index (FI). The error bar represents the range within which the mean FI fluctuates by up to 5%.

Lastly, our segmentation methods demonstrate a significant improvement over traditional segmentation methods, particularly in terms of handling complex features and high noise level images. Future work could focus on further refining the segmentation to further reduce over-segmentation and under-segmentation, potentially through the incorporation of advanced techniques such as deep learning and post-processing steps. Since various image segmentation methods are currently available and future advancements are anticipated, the micro-CT data provided in our study offers a chance for future comparison and further iterations.

5 Conclusions

This study introduces a non-destructive method for characterizing the lunar regolith sample returned by the CE-5 mission using micro-CT imaging and machine learning-based segmentation.

We generated and analyzed a comprehensive dataset of over 700,000 CE-5 lunar regolith particles, several orders of magnitude larger than previous studies, which significantly enhanced our ability to observe and characterize CE-5 lunar regolith particles. Our study indicates that the CE-5 samples have a median particle size of 57.5 μm, smaller than Apollo 11, Apollo 16, and Luna 24 samples. By comparing CE-5 lunar regolith particles with both terrestrial soils and other lunar samples, we revealed their less spherical shape with more complex morphological features.

Several pieces of evidence pointing to contradict maturity of the CE-5 lunar regolith. Compared to the previous lunar regolith sample, the smaller median particle size indicates higher maturity, however, the less spherical shape and the observed agglutinate suggest a relatively immature regolith. We recommend that due to the variability of the intrinsic crystal size of the protolith and the complexity of processes involved in space weathering, the relationship between lunar regolith particle size and morphology and maturity should be evaluated with caution, appealing further constraints to accurately assess the maturity of lunar regolith. In addition, we found that the samples should be sufficiently large (>1000) to obtain reliable shape and size characteristics. This study validates the feasibility and effectiveness of our proposed micro-CT imaging-based method on the examination of million scale exterritorial soils, which provides a non-destructive approach for assessing mineral components of precious extraterrestrial samples in future deep space explorations.

Acknowledgments

We appreciate the constructive suggestions and comments from the editor and the anonymous reviewers. Q. Zhao, H. Wu, and Y. Zou are supported by projects of the PolyU Research Centre for Deep Space Explorations (P0049221 and P0041304). B. Wu is supported by Research Grants Council of Hong Kong (RIF Project No: R5043-19W). W. Yang would like to thank the support from the National Natural Science Foundation of China (42241103) and the Key Research Program of Institute of Geology and Geophysics, Chinese Academy of Sciences (IGGCAS-202101).

References

Amrouche, M., Weber, R. C., Schmerr, N., & Iqbal, W. (2022). Effects of lunar near-surface geology on moonquakes ground motion amplification. *Journal of Geophysical Research: Planets*, *127*(9), e2022JE007396. https://doi.org/10.1029/2022JE007396

Anand, M., Taylor, L. A., Nazarov, M. A., Shu, J., Mao, H.-K., & Hemley, R. J. (2004). Space weathering on airless planetary bodies: Clues from the lunar mineral hapkeite. *Proceedings of the National Academy of Sciences*, *101*(18), 6847–6851. https://doi.org/10.1073/pnas.0401565101

Andres, B., Kappes, J. H., Beier, T., Köthe, U., & Hamprecht, F. A. (2011). Probabilistic image segmentation with closedness constraints. *2011 International Conference on Computer Vision*, 2611–2618. https://doi.org/10.1109/ICCV.2011.6126550

Blatt, H., Tracy, R., & Owens, B. (2006). *Petrology: Igneous, sedimentary, and metamorphic*. Macmillan.

Borg, L. E., Connelly, J. N., Boyet, M., & Carlson, R. W. (2011). Chronological evidence that the Moon is either young or did not have a global magma ocean. *Nature*, *477*(7362), Article 7362. https://doi.org/10.1038/nature10328

Breiman, L. (2001). Random forests. *Machine Learning*, *45*(1), 5–32. https://doi.org/10.1023/A:1010933404324

Cao, K., Dong, M., She, Z., Xiao, Q., Wang, X., Qian, Y., Li, Y., Wang, Z., He, Q., Wu, X., Zong, K., Hu, Z., & Xiao, L. (2022). A novel method for simultaneous analysis of particle size and mineralogy for Chang’E-5 lunar soil with minimum sample consumption. *Science China Earth Sciences*, *65*(9), 1704–1714. https://doi.org/10.1007/s11430-022-9966-5

Carrier III, W. D. (1973). Lunar soil grain size distribution. *The Moon*, *6*(3–4), 250–263. https://doi.org/10.1007/BF00562206

Carrier III, W. D., Bromwell, L. G., & Torrence Martin, R. (1972). Strength and compressibility of returned lunar soil. *Lunar and Planetary Science Conference Proceedings*, *3*, 3223.

Cavarretta, I., Coop, M., & O'Sullivan, C. (2010). The influence of particle characteristics on the behaviour of coarse grained soils. *Géotechnique*, *60*(6), 413–423. https://doi.org/10.1680/geot.2010.60.6.413

Chang, R., Lin, H., Yang, W., Ruan, R., Liu, X., Tian, H.-C., & Xu, J. (2023). Comparison of laboratory and in situ reflectance spectra of Chang'e-5 lunar soil. *Astronomy & Astrophysics*, *674*, A68. https://doi.org/10.1051/0004-6361/202245751

Chen, J., Zhao, C., Chen, Y., & Yang, Z. (2024). Effects of particle overall regularity and surface roughness on fabric evolution of granular materials: DEM simulations. *International Journal for Numerical and Analytical Methods in Geomechanics*, *48*(13), 3284–3307. https://doi.org/10.1002/nag.3792

Chen, Y., Hu, S., Li, J.-H., Li, Q.-L., Li, X., Li, Y., Liu, Y., Qian, Y., Yang, W., Zhou, Q., Lin, Y., Li, C., & Li, X.-H. (2023). Chang'e-5 lunar samples shed new light on the Moon. *The Innovation Geoscience*, 100014. https://doi.org/10.59717/j.xinn-geo.2023.100014

Chen, Y., Ma, G., Zhou, W., Wei, D., Zhao, Q., Zou, Y., & Grasselli, G. (2021). An enhanced tool for probing the microscopic behavior of granular materials based on X-ray micro-CT and FDEM. *Computers and Geotechnics*, *132*, 103974. https://doi.org/10.1016/j.compgeo.2020.103974

Chiaramonti, A. N., Goguen, J. D., & Garboczi, E. J. (2017). Quantifying the 3-dimensional shape of lunar regolith particles using X-ray computed tomography and scanning electron microscopy at sub-γ resolution. *Microscopy and Microanalysis*, *23*(S1), 2194–2195. https://doi.org/10.1017/S1431927617011631

Cho, G.-C., Dodds, J., & Santamarina, J. C. (2006). Particle shape effects on packing density, stiffness, and strength: Natural and crushed sands. *Journal of Geotechnical and Geoenvironmental Engineering*, *132*(5), 591–602. https://doi.org/10.1061/(ASCE)1090-0241(2006)132:5(591)

Colwell, J. E., Batiste, S., Horányi, M., Robertson, S., & Sture, S. (2007). Lunar surface: Dust dynamics and regolith mechanics. *Reviews of Geophysics*, *45*(2), 2005RG000184. https://doi.org/10.1029/2005RG000184

Costes, N. C., Cohron, G. T., & Moss, D. C. (1971). Cone penetration resistance test-an approach to evaluating in-place strength and packing characteristics of lunar soils. *Proceedings of the Lunar Science Conference, Vol. 2, p. 1973*, *2*, 1973.

Crook, K. A. W. (1968). Weathering and roundness of quartz sand grains. *Sedimentology*, *11*(3–4), 171–182. https://doi.org/10.1111/j.1365-3091.1968.tb00851.x

Deitrick, S. R., & Cannon, K. M. (2022). Characterizing detailed grain shape and size distribution properties of lunar regolith. *53rd Lunar and Planetary Science Conference*. https://ntrs.nasa.gov/citations/20210026714

Duke, M. B., Woo, C. C., Bird, M. L., Sellers, G. A., & Finkelman, R. B. (1970). Lunar soil: Size distribution and mineralogical constituents. *Science*, *167*(3918), 648–650. https://doi.org/10.1126/science.167.3918.648

Ellery, A. (2022). Leveraging in situ resources for lunar base construction. *Canadian Journal of Civil Engineering*, *49*(5), 657–674. https://doi.org/10.1139/cjce-2021-0098

Fujiwara, A., Kamimoto, G., & Tsukamoto, A. (1978). Expected shape distribution of asteroids obtained from laboratory impact experiments. *Nature*, *272*(5654), 602–603. https://doi.org/10.1038/272602a0

Garboczi, E. J. (2002). Three-dimensional mathematical analysis of particle shape using X-ray tomography and spherical harmonics: Application to aggregates used in concrete. *Cement and Concrete Research*, *32*(10), 1621–1638. https://doi.org/10.1016/S0008-8846(02)00836-0

Graf, J. C. (1993). *Lunar soils grain size catalog*. https://ntrs.nasa.gov/citations/19930012474

Gu, L., Chen, Y., Xu, Y., Tang, X., Lin, Y., Noguchi, T., & Li, J. (2022). Space weathering of the Chang'e-5 lunar sample from a mid-high latitude region on the Moon. *Geophysical Research Letters*, *49*(7), e2022GL097875. https://doi.org/10.1029/2022GL097875

Han, W., Ding, L., Cai, L., Zhu, J., Luo, H., & Tang, T. (2022). Sintering of HUST-1 lunar regolith simulant. *Construction and Building Materials*, *324*, 126655. https://doi.org/10.1016/j.conbuildmat.2022.126655

Hapke, B. W. (1968). On the particle size distribution of lunar soil. *Planetary and Space Science*, *16*(1), 101–110. https://doi.org/10.1016/0032-0633(68)90047-0

He, Q., Li, Y., Baziotis, I., Qian, Y., Xiao, L., Wang, Z., Zhang, W., Luo, B., Neal, C. R., Day, J. M. D., Pan, F., She, Z., Wu, X., Hu, Z., Zong, K., & Wang, L. (2022). Detailed petrogenesis of the unsampled Oceanus Procellarum: The case of the Chang'e-5 mare basalts. *Icarus*, *383*, 115082. https://doi.org/10.1016/j.icarus.2022.115082

Head, J. W., & Wilson, L. (2020). Rethinking lunar mare basalt regolith formation: New concepts of lava flow protolith and evolution of regolith thickness and internal structure.

Geophysical Research Letters, *47*(20), e2020GL088334. https://doi.org/10.1029/2020GL088334

Heiken, G., Vaniman, D., & French, B. M. (1991). *Lunar sourcebook: A user's guide to the Moon*. CUP Archive.

Hiebert, F. K., & Bennett, P. C. (1992). Microbial control of silicate weathering in organic-rich ground water. *Science*, *258*(5080), 278–281. https://doi.org/10.1126/science.258.5080.278

Huang, X., Qi, S., Xia, K., & Shi, X. (2018). Particle crushing of a filled fracture during compression and its effect on stress wave propagation. *Journal of Geophysical Research: Solid Earth*, *123*(7), 5559–5587. https://doi.org/10.1029/2018JB016001

Huang, X., Zhao, Q., Qi, S., Xia, K., Grasselli, G., & Chen, X. (2016). Numerical simulation on seismic response of the filled joint under high amplitude stress waves using finite-discrete element method (FDEM). *Materials*, *10*(1), 13. https://doi.org/10.3390/ma10010013

Humbert, L., Hazrati Marangalou, J., del Río Barquero, L. M., van Lenthe, G. H., & van Rietbergen, B. (2016). Technical note: Cortical thickness and density estimation from clinical CT using a prior thickness-density relationship. *Medical Physics*, *43*(4), 1945–1954. https://doi.org/10.1118/1.4944501

Katagiri, J., Matsushima, T., Yamada, Y., Tsuchiyama, A., Nakano, T., Uesugi, K., Ohtake, M., & Saiki, K. (2015). Investigation of 3D grain shape characteristics of lunar soil retrieved in Apollo 16 using image-based discrete-element modeling. *Journal of Aerospace Engineering*, *28*(4), 04014092. https://doi.org/10.1061/(ASCE)AS.1943-5525.0000421

La Spina, A., & Paolicchi, P. (1996). Catastrophic fragmentation as a stochastic process: Sizes and shapes of fragments. *Planetary and Space Science*, *44*(12), 1563–1578. https://doi.org/10.1016/S0032-0633(96)00064-5

Laczniak, D. L., Thompson, M. S., Christoffersen, R., Dukes, C. A., Clemett, S. J., Morris, R. V., & Keller, L. P. (2021). Characterizing the spectral, microstructural, and chemical effects of solar wind irradiation on the Murchison carbonaceous chondrite through coordinated analyses. *Icarus, 364*, 114479. https://doi.org/10.1016/j.icarus.2021.114479

Lee, C., Suh, H. S., Yoon, B., & Yun, T. S. (2017). Particle shape effect on thermal conductivity and shear wave velocity in sands. *Acta Geotechnica*, *12*(3), 615–625. https://doi.org/10.1007/s11440-017-0524-6

Lei, L., Seol, Y., & Jarvis, K. (2018). Pore-scale visualization of methane hydrate-bearing sediments with micro-CT. *Geophysical Research Letters*, *45*(11), 5417–5426. https://doi.org/10.1029/2018GL078507

Li, C., Hu, H., Yang, M.-F., Pei, Z.-Y., Zhou, Q., Ren, X., Liu, B., Liu, D., Zeng, X., Zhang, G., Zhang, H., Liu, J., Wang, Q., Deng, X., Xiao, C., Yao, Y., Xue, D., Zuo, W., Su, Y., … Ouyang, Z. (2022). Characteristics of the lunar samples returned by the Chang'E-5 mission. *National Science Review*, *9*(2), nwab188. https://doi.org/10.1093/nsr/nwab188

Li, C., Wang, C., Wei, Y., & Lin, Y. (2019). China's present and future lunar exploration program. *Science, 365*(6450), Article 6450. https://doi.org/10.1126/science.aax9908

Li, Q.-L., Zhou, Q., Liu, Y., Xiao, Z., Lin, Y., Li, J.-H., Ma, H.-X., Tang, G.-Q., Guo, S., Tang, X., Yuan, J.-Y., Li, J., Wu, F.-Y., Ouyang, Z., Li, C., & Li, X.-H. (2021). Two-billion-year-old volcanism on the Moon from Chang'e-5 basalts. *Nature, 600*(7887), Article 7887. https://doi.org/10.1038/s41586-021-04100-2

Longhi, J. (1992). Experimental petrology and petrogenesis of mare volcanics. *Geochimica et Cosmochimica Acta*, *56*(6), 2235–2251. https://doi.org/10.1016/0016-7037(92)90186-M

Lu, X., Chen, J., Ling, Z., Liu, C., Fu, X., Qiao, L., Zhang, J., Cao, H., Liu, J., He, Z., & Xu, R. (2023). Mature lunar soils from Fe-rich and young mare basalts in the Chang'e-5 regolith samples. *Nature Astronomy*, *7*(2), 142–151. https://doi.org/10.1038/s41550-022-01838-1

Matsushima, T., Katagiri, J., Saiki, K., Tsuchiyama, A., Ohtake, M., Nakano, T., & Uesugi, K. (2008). 3D particle characteristics of highland lunar soil (No. 60501) obtained by micro X-ray CT. In *Earth & Space 2008: Engineering, Science, Construction, and Operations in Challenging Environments* (pp. 1–8).

McCusker, L. B., Von Dreele, R. B., Cox, D. E., Louër, D., & Scardi, P. (1999). Rietveld refinement guidelines. *Journal of Applied Crystallography*, *32*(1), 36–50. https://doi.org/10.1107/S0021889898009856

McKay, D. S., Fruland, R. M., & Heiken, G. H. (1974). Grain size and the evolution of lunar soils. *In: Lunar Science Conference, 5th, Houston, Tex., March 18-22, 1974, Proceedings. Volume 1.(A75-39540 19-91) New York, Pergamon Press, Inc., 1974, p. 887-906.*, *5*, 887–906. https://adsabs.harvard.edu/full/record/seri/LPSC./0005/1974LPSC....5..887M.html

Meyer, F., & Beucher, S. (1990). Morphological segmentation. *Journal of Visual Communication and Image Representation*, *1*(1), 21–46. https://doi.org/10.1016/1047-3203(90)90014-M

Michikami, T., Kadokawa, T., Tsuchiyama, A., Hagermann, A., Nakano, T., Uesugi, K., & Hasegawa, S. (2018). Influence of petrographic textures on the shapes of impact experiment fine fragments measuring several tens of microns: Comparison with Itokawa regolith particles. *Icarus*, *302*, 109–125. https://doi.org/10.1016/j.icarus.2017.10.040

Morota, T., Haruyama, J., Ohtake, M., Matsunaga, T., Honda, C., Yokota, Y., Kimura, J., Ogawa, Y., Hirata, N., Demura, H., Iwasaki, A., Sugihara, T., Saiki, K., Nakamura, R., Kobayashi, S., Ishihara, Y., Takeda, H., & Hiesinger, H. (2011). Timing and characteristics of the latest mare eruption on the Moon. *Earth and Planetary Science Letters*, *302*(3), 255–266. https://doi.org/10.1016/j.epsl.2010.12.028

Nie, J., Cui, Y., Senetakis, K., Guo, D., Wang, Y., Wang, G., Feng, P., He, H., Zhang, X., Zhang, X., Li, C., Zheng, H., Hu, W., Niu, F., Liu, Q., & Li, A. (2023). Predicting residual friction angle of lunar regolith based on Chang'e-5 lunar samples. *Science Bulletin*, *68*(7), 730–739. https://doi.org/10.1016/j.scib.2023.03.019

Otsu, N. (1979). A threshold selection method from gray-level histograms. *IEEE Transactions on Systems, Man, and Cybernetics*, *9*(1), 62–66. https://doi.org/10.1109/TSMC.1979.4310076

Perkins, S. W., & Madson, C. R. (1996). Mechanical and load-settlement characteristics of two lunar soil simulants. *Journal of Aerospace Engineering*, *9*(1), 1–9. https://doi.org/10.1061/(ASCE)0893-1321(1996)9:1(1)

Qian, Y., She, Z., He, Q., Xiao, L., Wang, Z., Head, J. W., Sun, L., Wang, Y., Wu, B., Wu, X., Luo, B., Cao, K., Li, Y., Dong, M., Song, W., Pan, F., Michalski, J., Ye, B., Zhao, J., … Hu, Z. (2023). Mineralogy and chronology of the young mare volcanism in the Procellarum-KREEP-Terrane. *Nature Astronomy*, *7*(3), Article 3. https://doi.org/10.1038/s41550-022-01862-1

Qian, Y., Xiao, L., Wang, Q., Head, J. W., Yang, R., Kang, Y., van der Bogert, C. H., Hiesinger, H., Lai, X., Wang, G., Pang, Y., Zhang, N., Yuan, Y., He, Q., Huang, J., Zhao, J., Wang, J., & Zhao, S. (2021). China's Chang'e-5 landing site: Geology, stratigraphy, and provenance of materials. *Earth and Planetary Science Letters*, *561*, 116855. https://doi.org/10.1016/j.epsl.2021.116855

Qian, Y., Xiao, L., Yin, S., Zhang, M., Zhao, S., Pang, Y., Wang, J., Wang, G., & Head, J. W. (2020). The regolith properties of the Chang'e-5 landing region and the ground drilling experiments using lunar regolith simulants. *Icarus*, *337*, 113508. https://doi.org/10.1016/j.icarus.2019.113508

Qian, Y., Xiao, L., Zhao, J., Head, J. W., He, Q., Xu, H., Wang, F., Zhang, X., Ping, X., Zeng, W., Wang, X., Michalski, J., Liu, J., Ye, B., Wang, M., Sun, L., Pang, Y., Wang, J., & Zhao, S. (2024). First magnetic and spectroscopic constraints on attenuated space weathering at the Chang'e-5 landing site. *Icarus*, *410*, 115892. https://doi.org/10.1016/j.icarus.2023.115892

Qianqian Fang, & Boas, D. A. (2009). Tetrahedral mesh generation from volumetric binary and grayscale images. *2009 IEEE International Symposium on Biomedical Imaging: From Nano to Macro*, 1142–1145. https://doi.org/10.1109/ISBI.2009.5193259

Rousé, P. C., Fannin, R. J., & Shuttle, D. A. (2008). Influence of roundness on the void ratio and strength of uniform sand. *Géotechnique*, *58*(3), 227–231. https://doi.org/10.1680/geot.2008.58.3.227

Russ, J. C. (2013). *Fractal surfaces*. Springer Science & Business Media.

Schmitt, H. H., Petro, N. E., Wells, R. A., Robinson, M. S., Weiss, B. P., & Mercer, C. M. (2017). Revisiting the field geology of Taurus–Littrow. *Icarus*, *298*, 2–33. https://doi.org/10.1016/j.icarus.2016.11.042

Shen, L., Farid, H., & McPeek, M. A. (2009). Modeling three-dimensional morphological structures using spherical harmonics. *Evolution*, *63*(4), 1003–1016. https://doi.org/10.1111/j.1558-5646.2008.00557.x

Shotton, J., Johnson, M., & Cipolla, R. (2008). Semantic texton forests for image categorization and segmentation. *2008 IEEE Conference on Computer Vision and Pattern Recognition*, 1–8. https://doi.org/10.1109/CVPR.2008.4587503

Smith, M., Craig, D., Herrmann, N., Mahoney, E., Krezel, J., McIntyre, N., & Goodliff, K. (2020). The Artemis program: An overview of NASA's activities to return humans to the Moon. *2020 IEEE Aerospace Conference*, 1–10. https://doi.org/10.1109/AERO47225.2020.9172323

Snape, J. F., Nemchin, A. A., Whitehouse, M. J., Merle, R. E., Hopkinson, T., & Anand, M. (2019). The timing of basaltic volcanism at the Apollo landing sites. *Geochimica et Cosmochimica Acta*, *266*, 29–53. https://doi.org/10.1016/j.gca.2019.07.042

Sommer, C., Straehle, C., Koethe, U., & Hamprecht, F. A. (2011). Ilastik: Interactive learning and segmentation toolkit. *2011 IEEE International Symposium on Biomedical Imaging: From Nano to Macro*, 230–233. https://doi.org/10.1109/ISBI.2011.5872394

Steiglitz, R. D. (1988). Rock particles, fragments. In *General Geology* (pp. 711–716). Kluwer Academic Publishers. https://doi.org/10.1007/0-387-30844-X_96

Sudhyadhom, A. (2020). On the molecular relationship between Hounsfield Unit (HU), mass density, and electron density in computed tomography (CT). *PLOS ONE*, *15*(12), e0244861. https://doi.org/10.1371/journal.pone.0244861

Thompson, M. S., Zega, T. J., Becerra, P., Keane, J. T., & Byrne, S. (2016). The oxidation state of nanophase Fe particles in lunar soil: Implications for space weathering. *Meteoritics & Planetary Science*, *51*(6), 1082–1095. https://doi.org/10.1111/maps.12646

Tian, H.-C., Wang, H., Chen, Y., Yang, W., Zhou, Q., Zhang, C., Lin, H.-L., Huang, C., Wu, S.-T., Jia, L.-H., Xu, L., Zhang, D., Li, X.-G., Chang, R., Yang, Y.-H., Xie, L.-W., Zhang, D.-P., Zhang, G.-L., Yang, S.-H., & Wu, F.-Y. (2021). Non-KREEP origin for Chang'e-5 basalts in the Procellarum KREEP Terrane. *Nature, 600*(7887), Article 7887. https://doi.org/10.1038/s41586-021-04119-5

Tomioka, N., & Fujino, K. (1997). Natural $(Mg,Fe)SiO_3$ -ilmenite and -perovskite in the Tenham meteorite. *Science, 277*(5329), 1084–1086. https://doi.org/10.1126/science.277.5329.1084

Tsuchiyama, A., Sakurama, T., Nakano, T., Uesugi, K., Ohtake, M., Matsushima, T., Terakado, K., & Galimov, E. M. (2022). Three-dimensional shape distribution of lunar regolith particles collected by the Apollo and Luna programs. *Earth, Planets and Space*, *74*(1), 172. https://doi.org/10.1186/s40623-022-01737-9

Watters, T. R., Weber, R. C., Collins, G. C., Howley, I. J., Schmerr, N. C., & Johnson, C. L. (2019). Shallow seismic activity and young thrust faults on the Moon. *Nature Geoscience*, *12*(6), 411–417. https://doi.org/10.1038/s41561-019-0362-2

Weber, I., Stojic, A. N., Morlok, A., Reitze, M. P., Markus, K., Hiesinger, H., Pavlov, S. G., Wirth, R., Schreiber, A., Sohn, M., Hübers, H.-W., & Helbert, J. (2020). Space weathering by simulated micrometeorite bombardment on natural olivine and pyroxene: A coordinated IR and TEM study. *Earth and Planetary Science Letters*, *530*, 115884. https://doi.org/10.1016/j.epsl.2019.115884

Wei, D., Wang, J., Nie, J., & Zhou, B. (2018). Generation of realistic sand particles with fractal nature using an improved spherical harmonic analysis. *Computers and Geotechnics*, *104*, 1–12. https://doi.org/10.1016/j.compgeo.2018.08.002

Wei, D., Wang, J., & Zhao, B. (2018). A simple method for particle shape generation with spherical harmonics. *Powder Technology*, *330*, 284–291. https://doi.org/10.1016/j.powtec.2018.02.006

Wieczorek, M. A. (2006). The constitution and structure of the lunar interior. *Reviews in Mineralogy and Geochemistry*, *60*(1), 221–364. https://doi.org/10.2138/rmg.2006.60.3

Wilkerson, R. P., Rickman, D. L., McElderry, J. R., Walker, S. R., & Cannon, K. M. (2024). On the measurement of shape: With applications to lunar regolith. *Icarus*, *412,* 115963. https://doi.org/10.1016/j.icarus.2024.115963

Woods-Robinson, R., Siegler, M. A., & Paige, D. A. (2019). A model for the thermophysical properties of lunar regolith at low temperatures. *Journal of Geophysical Research: Planets*, *124*(7), 1989–2011. https://doi.org/10.1029/2019JE005955

Wu, B., Huang, J., Li, Y., Wang, Y., & Peng, J. (2018). Rock abundance and crater density in the candidate Chang’e-5 landing region on the Moon. *Journal of Geophysical Research: Planets*, *123*(12), 3256–3272. https://doi.org/10.1029/2018JE005820

Wu, F.-Y., Li, Q.-L., Chen, Y., Hu, S., Yue, Z.-Y., Zhou, Q., Wang, H., Yang, W., Tian, H., Zhang, C., Li, J.-H., Li, L.-X., Hui, H.-J., Lin, Y.-T., Li, X.-H., & Delano, J. (2024).

Lunar evolution in light of the Chang'e-5 returned samples. *Annual Review of Earth and Planetary Sciences*, *52*. https://doi.org/10.1146/annurev-earth-040722-100453

Xian, H., Zhu, J., Yang, Y., Li, S., Lin, X., Xi, J., Xing, J., Wu, X., Yang, H., Zhou, Q., Tsuchiyama, A., He, H., & Xu, Y.-G. (2023). Ubiquitous and progressively increasing ferric iron content on the lunar surfaces revealed by the Chang'e-5 sample. *Nature Astronomy*, *7*(3), Article 3. https://doi.org/10.1038/s41550-022-01855-0

Xiao, Y., Yuan, Z., Chu, J., Liu, H., Huang, J., Luo, S. N., Wang, S., & Lin, J. (2019). Particle breakage and energy dissipation of carbonate sands under quasi-static and dynamic compression. *Acta Geotechnica*, *14*(6), 1741–1755. https://doi.org/10.1007/s11440-019-00790-1

Xie, H. (2020). *Fractals in rock mechanics*. CRC Press. https://doi.org/10.1201/9781003077626

Yang, W., Chen, Y., Wang, H., Tian, H., Hui, H., Xiao, Z., Wu, S., Zhang, D., Zhou, Q., Ma, H., Zhang, C., Hu, S., Li, Q., Lin, Y., Li, X.-H., & Wu, F.-Y. (2022). Geochemistry of impact glasses in the Chang'e-5 regolith: Constraints on impact melting and the petrogenesis of local basalt. *Geochimica et Cosmochimica Acta*, *335*. https://doi.org/10.1016/j.gca.2022.08.030

Yang, W., & Lin, Y. (2021). New lunar samples returned by Chang'e-5: Opportunities for new discoveries and international collaboration. *The Innovation*, *2*(1), 100070. https://doi.org/10.1016/j.xinn.2020.100070

Yang, Y., Jiang, T., Liu, Y., Xu, Y., Zhang, H., Tian, H.-C., Yang, W., & Zou, Y. (2022). A micro mid-infrared spectroscopic study of Chang'e-5 sample. *Journal of Geophysical Research: Planets*, *127*(8), e2022JE007453. https://doi.org/10.1029/2022JE007453

Yao, Y., Xiao, C., Wang, P., Li, C., & Zhou, Q. (2022). Instrumental neutron activation analysis of Chang'e-5 lunar regolith samples. *Journal of the American Chemical Society*, *144*(12), 5478–5484. https://doi.org/10.1021/jacs.1c13604

Zhang, H., Zhang, X., Zhang, G., Dong, K., Deng, X., Gao, X., Yang, Y., Xiao, Y., Bai, X., Liang, K., Liu, Y., Ma, W., Zhao, S., Zhang, C., Zhang, X., Song, J., Yao, W., Chen, H., Wang, W., … Yang, M. (2022). Size, morphology, and composition of lunar samples returned by Chang'E-5 mission. *Science China Physics, Mechanics & Astronomy*, *65*(2), Article 2. https://doi.org/10.1007/s11433-021-1818-1

Zhang, M., Fa, W., & Eke, V. R. (2023). Modeling the evolution of lunar regolith: 1. Formation mechanism through individual simple impact craters. *Journal of Geophysical Research: Planets*, *128*(8), e2023JE007850. https://doi.org/10.1029/2023JE007850

Zhao, B., & Wang, J. (2015). 3D quantitative shape analysis on form, roundness, and compactness with μCT. *Powder Technology*, *291*. https://doi.org/10.1016/j.powtec.2015.12.029

Zhao, B., Wang, J., Andò, E., Viggiani, G., & Coop, M. R. (2020). Investigation of particle breakage under one-dimensional compression of sand using X-ray microtomography. *Canadian Geotechnical Journal*, *57*(5), 754–762. https://doi.org/10.1139/cgj-2018-0548

Zhou, B., Wang, J., & Zhao, B. (2015). Micromorphology characterization and reconstruction of sand particles using micro X-ray tomography and spherical harmonics. *Engineering Geology*, *184*, 126–137. https://doi.org/10.1016/j.enggeo.2014.11.009

Zhu, F., & Zhao, J. (2021). Interplays between particle shape and particle breakage in confined continuous crushing of granular media. *Powder Technology*, *378*, 455–467. https://doi.org/10.1016/j.powtec.2020.10.020

Zingg, T. (1935). *Beitrag zur schotteranalyse* [PhD Thesis]. ETH Zurich.

Zong, K., Wang, Z., Li, J., He, Q., Li, Y., Becker, H., Zhang, W., Hu, Z., He, T., Cao, K., She, Z., Wu, X., Xiao, L., & Liu, Y. (2022). Bulk compositions of the Chang'E-5 lunar soil: Insights into chemical homogeneity, exotic addition, and origin of landing site basalts. *Geochimica et Cosmochimica Acta*, *335*, 284–296. https://doi.org/10.1016/j.gca.2022.06.037